ERDC/GSL TR-22-4

Geotechnical and Structures Laboratory

US Army Corps
of Engineers®
Engineer Research and
Development Center

ERDC
ENGINEER RESEARCH & DEVELOPMENT CENTER

Full-Scale Evaluation of Multi-axial Geogrids in Road Applications

W. Jeremy Robinson

March 2022

Approved for public release; distribution is unlimited.

The U.S. Army Engineer Research and Development Center (ERDC) solves the nation's toughest engineering and environmental challenges. ERDC develops innovative solutions in civil and military engineering, geospatial sciences, water resources, and environmental sciences for the Army, the Department of Defense, civilian agencies, and our nation's public good. Find out more at www.erdc.usace.army.mil.

To search for other technical reports published by ERDC, visit the ERDC online library at https://erdclibrary.on.worldcat.org/discovery.

ERDC/GSL TR-22-4
March 2022

Full-scale Evaluation of Multi-axial Geogrids in Road Applications

W. Jeremy Robinson

Geotechnical and Structures Laboratory
U.S. Army Engineer Research and Development Center
3909 Halls Ferry Road
Vicksburg, MS 39180-6199

Final report

Approved for public release; distribution is unlimited.

Prepared for Tensar International Corporation
Alpharetta, GA 30009-2249

Under Work Unit 151098, Funding Account Code 887K5B

Abstract

The U.S. Army Engineer Research and Development Center (ERDC) constructed a full-scale unsurfaced test section to evaluate the performance of two prototype geogrids, referred to as NX950 and NX750, in road applications. The test section consisted of a 10-in.-thick crushed aggregate surface layer placed over a very weak 2 California Bearing Ratio (CBR) clay subgrade. Simulated truck traffic was applied using one of ERDC's specially designed load carts outfitted with a single-axle dual wheel truck gear. Rutting performance and instrumentation response data were monitored at multiple traffic intervals. It was found that the prototype geogrids improved rutting performance when compared to the unstabilized test item, and that the test item containing NX950 had the best rutting performance. Further, instrumentation response data indicated that the geogrids reduced measured pressure and deflection near the surface of the subgrade layer. Pressure response data in the aggregate layer suggested that the geogrids redistributed applied pressure higher in the aggregate layer, effectively changing the measured stress profile with an increase in pavement depth.

DISCLAIMER: The contents of this report are not to be used for advertising, publication, or promotional purposes. Citation of trade names does not constitute an official endorsement or approval of the use of such commercial products. All product names and trademarks cited are the property of their respective owners. The findings of this report are not to be construed as an official Department of the Army position unless so designated by other authorized documents.

DESTROY THIS REPORT WHEN NO LONGER NEEDED. DO NOT RETURN IT TO THE ORIGINATOR.

Contents

Figures and Tables

Figures

Tables

Preface

This study was conducted under Work Unit 151098, Funding Account Code 887K5B, for Tensar International Corporation located in Alpharetta, GA. Dr. Mark H. Wayne, Tensar, provided technical guidance and review during the project.

The work was performed by the Airfields and Pavements Branch (GMA) of the Engineering Systems and Materials Division (GM), U.S. Army Engineer Research and Development Center, Geotechnical and Structures Laboratory (ERDC-GSL). At the time of publication, Ms. Anna M. Jordan was Chief, GMA; Mr. Justin S. Strickler was Chief, GM; and Ms. Pamela G. Kinnebrew, GZ-T, was the Technical Director for Military Engineering. The Deputy Director of ERDC-GSL was Mr. Charles W. Ertle II, and the Director was Mr. Bartley P. Durst.

COL Teresa A. Schlosser was the Commander of ERDC, and Dr. David W. Pittman was the Director.

1 Introduction

1.1 Background

Since the 1990s, Tensar International Corporation (Tensar) has engaged the U.S. Army Engineer Research and Development Center (ERDC) to perform full-scale evaluations of prototype geogrid products. These evaluations have been used to determine the performance implications of incorporating geogrids in both flexible and unsurfaced pavement structures subjected to simulated highway loading conditions. Additionally, instrumentation response data have been used to validate Tensar's mechanistic-empirical pavement performance models. Thus, ERDC and Tensar have a long-standing history of performance testing that can be leveraged as newer prototype geogrids are developed.

1.2 Objective

The technical objective of this effort was to construct and traffic a full-scale unsurfaced pavement section that included an unstabilized control item and two geogrid-stabilized test items. Each stabilized test item included a prototype multi-axial geogrid located at the aggregate/subgrade interface. The test items that were evaluated had similar pavement layer thicknesses to previous unstabilized and stabilized unsurfaced pavement sections, which allowed for an expansion of historical observations and meaningful performance comparisons. Pavement performance was measured in terms of rutting in the primary traffic path, where rutting included upheaval outside the wheel path. A secondary objective was to record and analyze instrumentation response data for the verification of mechanistic performance models implemented within Tensar's SpectraPave4Pro™ pavement design software.

1.3 Scope

The scope of this project included the construction and trafficking of a full-scale test section comprised of a geogrid-stabilized aggregate layer. The ERDC constructed the full-scale test section under shelter in the Hangar 2 Pavement Test Facility. During construction, quality-control data were collected to verify layer properties and to ensure that project objectives were accomplished. The test items were fully instrumented to gather pavement response data under simulated single-axle dual wheel truck loading

conditions. Pavement performance data were collected at selected intervals during trafficking to compare the performance of the prototype multi-axial geogrids to each other as well as to the unstabilized control test item.

2 Test Plan and Layout

A large full-scale test section was constructed under cover in Hangar 2 at ERDC to evaluate the performance of multiaxial geogrids in road applications. Construction under cover minimized the influence of soil moisture changes due to inclement weather, i.e., rain events, for the duration of the test.

The structural design of the test section was developed by Tensar Corporation. Test items were constructed utilizing similar materials and construction techniques as previous experiments (Norwood and Tingle 2014; Robinson et. al. 2017) to extend the usefulness of performance comparisons. The full-scale test section included three individual test items that consisted of an unstabilized control and two geogrid test items, each stabilized with a different prototype geogrid. Each test item was 12.5 ft wide by 30 ft long. The test items were constructed with a nominal 24-in.-thick high-plasticity (CH) clay subgrade placed to achieve a target California Bearing Ratio (CBR) value of 2%. The test items were surfaced with a 10-in.-thick high-quality crushed limestone placed in one lift, thus mimicking typical construction practices over extremely soft subgrades where the primary purpose is to bridge over the soft layer in order to mitigate the potential for pumping in the aggregate layer. Figure 1 shows a plan view of the full-scale test section.

Figure 1. Test section plan view.

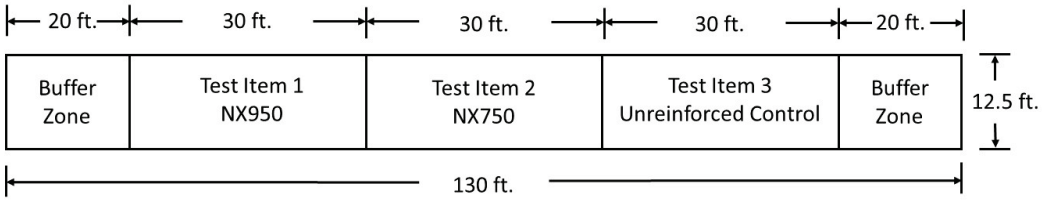

The test items contained a host of instrumentation that consisted of earth pressure cells, single-depth deflectometers, geogrid uniaxial strain gauges, bender elements, moisture probes, pore-water pressure transducers, and temperature probes. Instrumentation is discussed in detail in Chapter 4.

Simulated truck traffic was applied using one of ERDC's specially designed load carts outfitted with a single-axle dual-wheel truck gear. The single-axle dual-wheel truck gear was subjected to a 10,000-lb total load at a tire inflation pressure of 120 psi. The equivalent single-axle

load factor for this configuration is 1.51; thus, one pass of the load cart was equal to 1.51 equivalent single axle loads (ESALS). It should be noted here that 1.0 ESAL was defined as an 18,000-lb total single axle load on a dual-wheel truck gear (Huang 2004).

Traffic was applied such that 8 total passes comprised a full pattern (Figure 2) to the test area. When the test item centerline is considered, the applied traffic pattern resulted in 4 coverages, yielding a pass/coverage ratio 8 passes/4 coverages or 2.0.

Figure 2. Wander pattern used to apply simulated traffic.

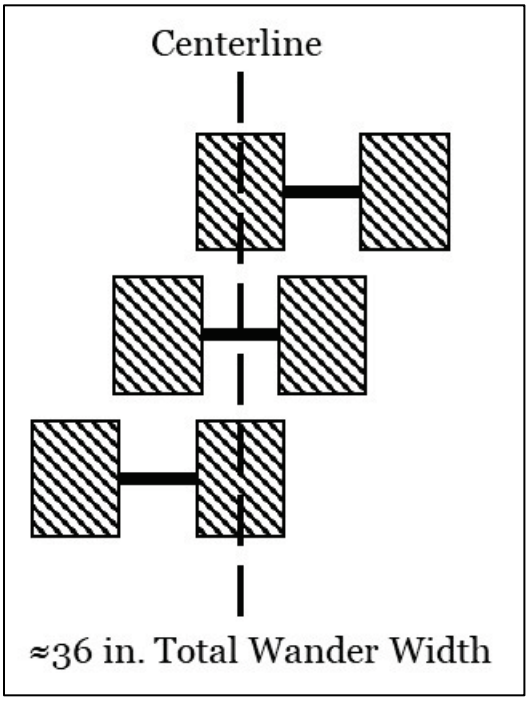

3 Materials

Laboratory tests were performed to characterize each component layer material as well as underlying subgrade soils. Material characterization test results are presented in the following paragraphs.

3.1 Subgrade

In-situ subgrade soils encountered at the bottom of the excavation consisted of a low-plasticity clay. A No. 200 wash test indicated that the material consisted of 7.1% sand and 92.9% fines. The soil had a liquid limit (LL) of 41%, a plastic limit (PL) of 22%, and a plasticity index (PI) of 19%. Modified Proctor compaction tests (ASTM D1557) indicated maximum dry density was 116.3 pcf at an optimum moisture content of 13.5% (Figure 3) (ASTM 2012). The dynamic cone penetrometer test indicated the in-situ subgrade soils had a CBR of approximately 15.

Figure 3. In-situ subgrade moisture/density relationship.

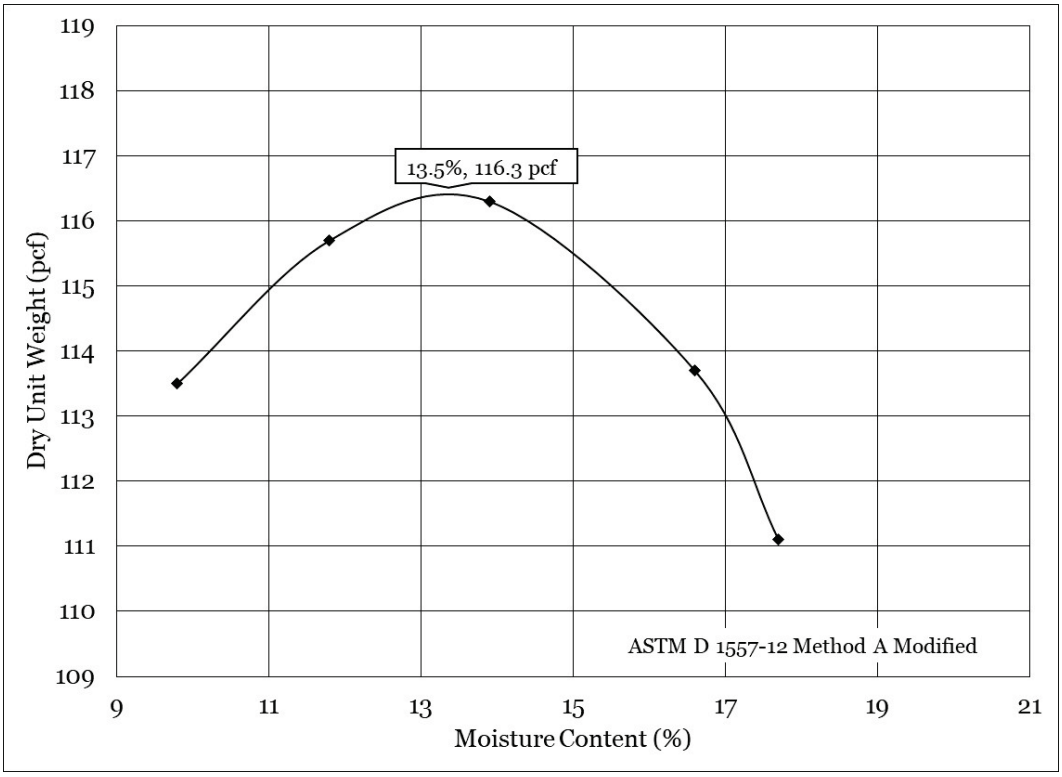

Design subgrade soils consisted of a locally sourced high-plasticity clay, commonly referred to as Vicksburg Buckshot. This material has been used extensively in test section construction, namely for its ability to maintain

moisture content (and, consequently, design strength) over an extended time period. A particle size analysis indicated the material consisted of 96.8% fines passing the No. 200 sieve. The soil had a LL of 85%, a PL of 29%, and a PI of 56% as determined by American Society for Testing and Materials (ASTM) D4318 2017c. According to the Unified Soil Classification System (USCS [ASTM 2017a]), the soil was classified as a high-plasticity clay (CH) and an A-7-6 according to the American Association of State and Highway Transportation Officials (AASHTO) classification system (2012).

Modified Proctor compaction tests (ASTM D1557) were performed to determine the relationship between moisture content and dry density. Maximum dry density was found to be 106.1 pcf at an optimum moisture content of 17.5% (ASTM 2012). Graphical results of the moisture-density relationship test are shown in Figure 4.

Figure 4. Clay subgrade moisture/density relationship.

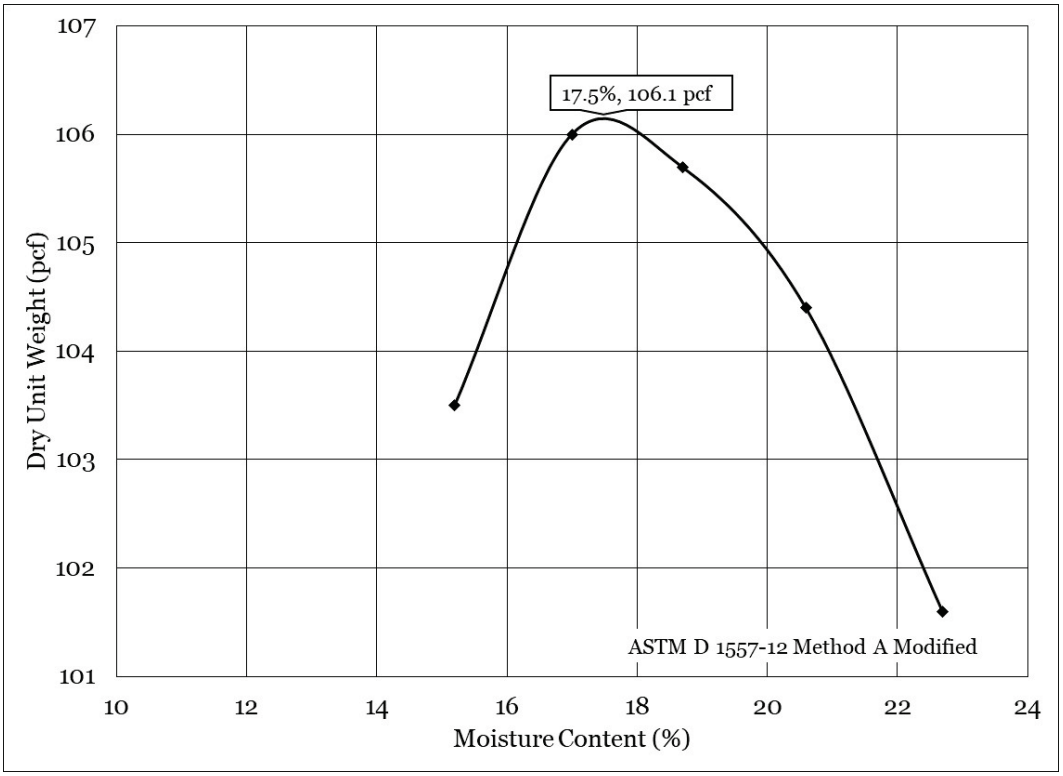

To determine an in-place moisture content at the targeted 2 CBR, a suite of laboratory CBR tests (ASTM D1883) was performed (ASTM 2016). These tests were conducted at moisture contents ranging from approximately 20% to approximately 40%. A target in-place moisture

content of 40% was selected based on the relationship between moisture content and CBR. The relationship between CBR and moisture content is presented graphically in Figure 5.

Figure 5. Clay subgrade CBR/moisture content relationship.

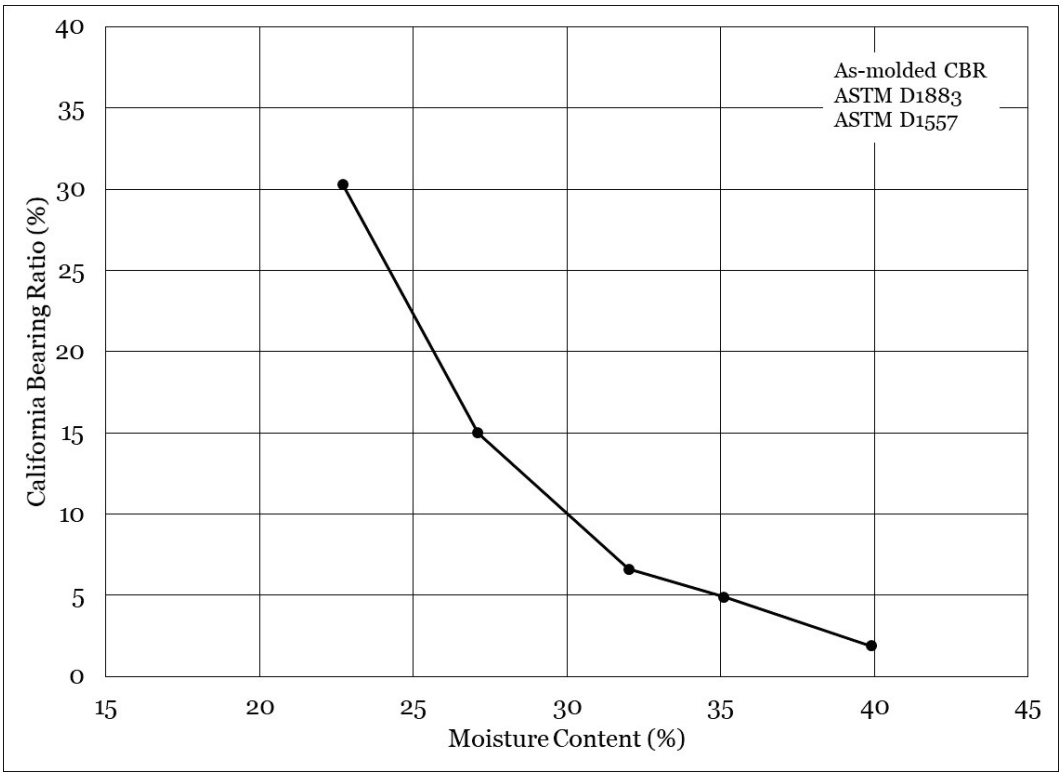

3.2 Aggregate surface

Crushed limestone (LMS) was used to construct the aggregate surface course. Crushed limestone was selected to represent a strong aggregate (historically this material yields an in-situ CBR of 80 to 100) that may be indicative of an aggregate used in a low-volume road application.

The gradation for the crushed limestone base is shown in Figure 6. ASTM procedure D2487 was used to determine that the base course was comprised of 66.2% gravel, 25.3% sand, and 8.5% non-plastic fines passing the No. 200 sieve (ASTM 2017a). The coefficient of curvature (Cc) was calculated as 7.63, and the coefficient of uniformity (Cu) was 68.21. The crushed limestone aggregate base was classified as a poorly graded gravel with silt and sand (GP-GM) according to the USCS (ASTM 2017a) and an A-1-a according to the AASHTO procedure (2012). Modified Proctor compaction tests (Figure 7) were performed in accordance with

ASTM D1557 Method C Modified (2012). The maximum dry density was 147.9 pcf at an optimum moisture content of 5.2%.

3.3 Geogrids

The geogrids evaluated in this study were manufactured from a coextruded, composite polymer sheet, which was then punched and oriented. The resulting structure consisted of continuous and non-continuous ribs forming three aperture geometries, i.e., hexagon, trapezoid, and triangle, and an unimpeded suspended hexagon. The geogrids had differing aperture sizes allowing the geogrids to interlock with a variety of aggregate sizes. Products evaluated previously have consisted of single-size apertures, thus it was hypothesized that the prototype geogrids would have enhanced aggregate stiffening capabilities attributed to improved aggregate interlock. The prototype geogrids were shipped to ERDC and remained in a storage area prior to installation in the test section. An abundance of material length was provided, and each product was trimmed to approximately 36 ft long to accommodate the 30-ft-long test section and allow for an approximate 3-ft-long overlap on each end. Nominal index properties (as provided by Tensar) for each geogrid are presented in Table 1.

Figure 6. Surface aggregate particle size analysis.

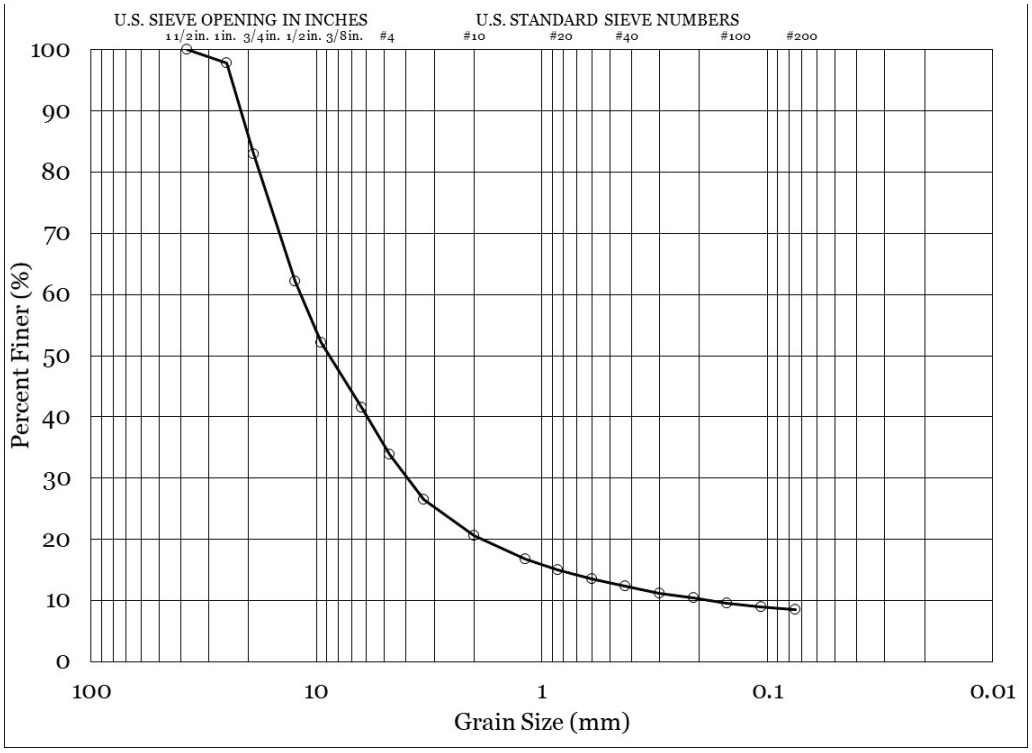

Figure 7. Surface aggregate moisture/density relationship.

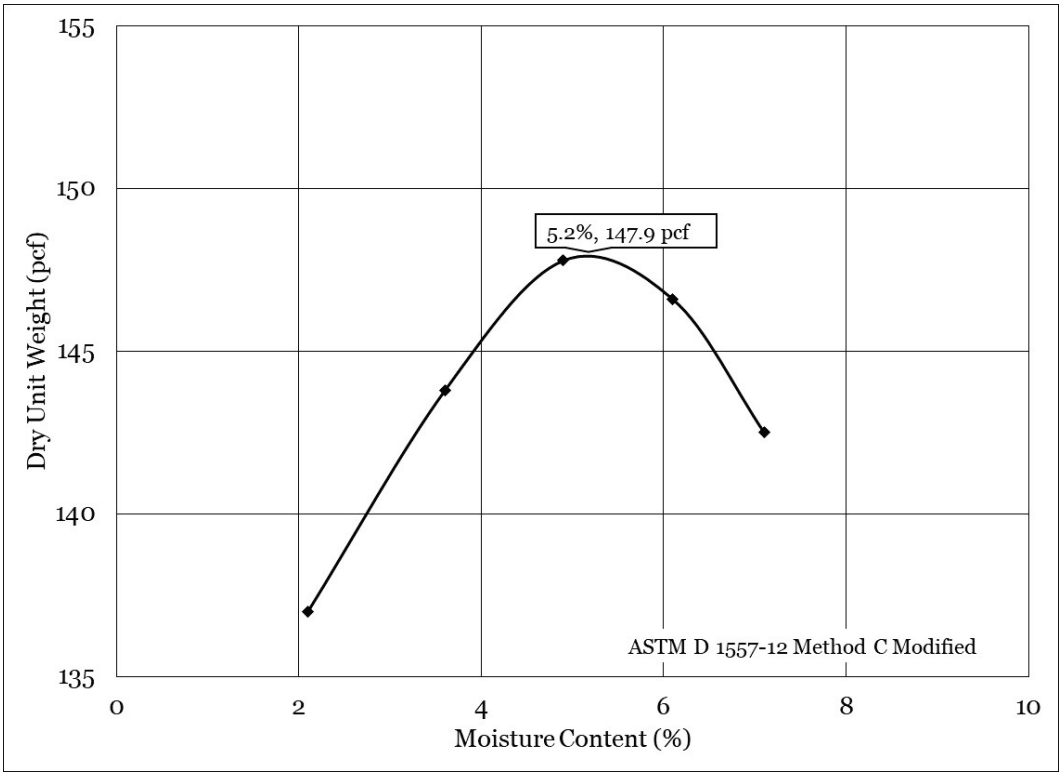

Table 1. Prototype geogrid dimensions.

Dimension	Rib Length (mm)					Aperture Size (mm)						Rib Width (mm)					Rib Height (mm)				
Sample Designation	A	B	C	D	E	AB	AD	BB	DD	EE	AAA	A	B	C	D	E	A	B	C	D	E
NX950	45	17	29	20	27	24	24	30	33	39	38	1.44	2.52	1.61	1.72	1.90	3.46	1.85	3.52	3.20	2.38
NX750	45	19	28	19	26	24	23	30	33	41	40	1.40	1.51	1.41	1.59	1.62	2.28	1.62	2.33	2.32	2.06
Note: Geogrid dimensions provided by Tensar																					

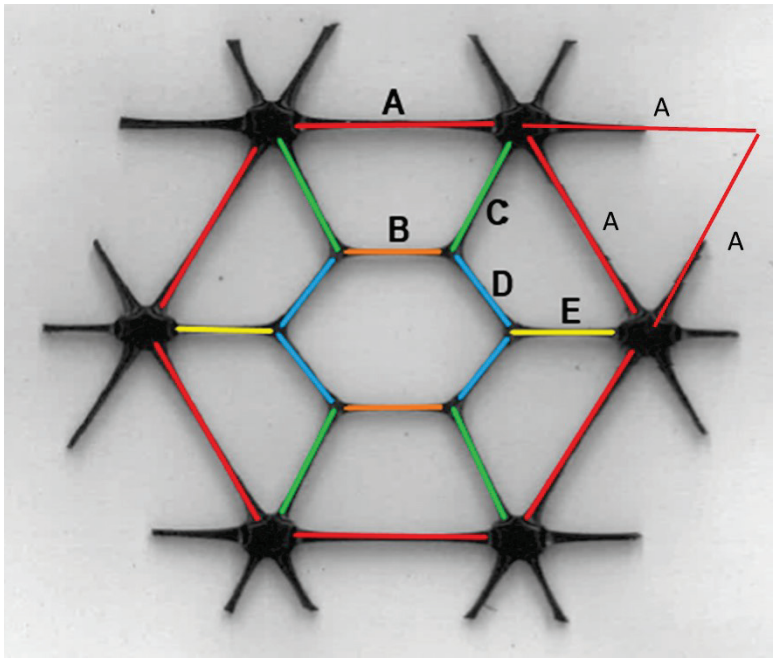

4 Instrumentation

Sensors were installed in the subgrade, in the aggregate layer, and on the geogrids to monitor pavement response during test section trafficking. Sensors used to capture the pavement response included earth pressure cells (EPCs), single-depth deflectometers (SDDs), uniaxial strain gauges (USGs), and bender elements (BEs). Pore-water pressure, temperature sensors, and moisture sensors were installed to monitor environmental parameters. Figures 8 and 9 show the plan and profile views, respectively, of the typical instrumentation layout for a test item.

Figure 8. Instrumentation plan view (typical).

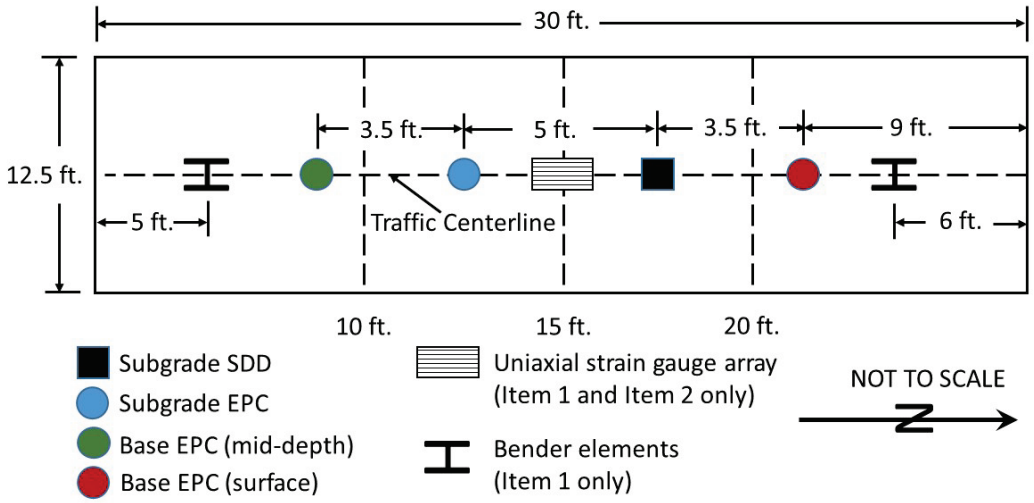

4.1 Earth pressure cells

Vertical stresses in the base course and subgrade were measured by using 9-in.-diam Geokon EPCs. EPCs provide a quantitative measurement of the vertical distribution of the stresses within each test item during testing. Earth pressure cells with a maximum pressure range up to 100 psi were installed in the subgrade, and 145-psi EPCs were installed in the base course. The EPCs in the base course were located approximately 2 in. above the subgrade/base interface and at mid-depth of the base layer, while the EPCs placed in the subgrade were located 2 in. below the top of the subgrade. Figure 10 shows an EPC being installed 2 in. below the surface of the subgrade at the interface with the base course.

Figure 9. Instrumentation profile view (typical).

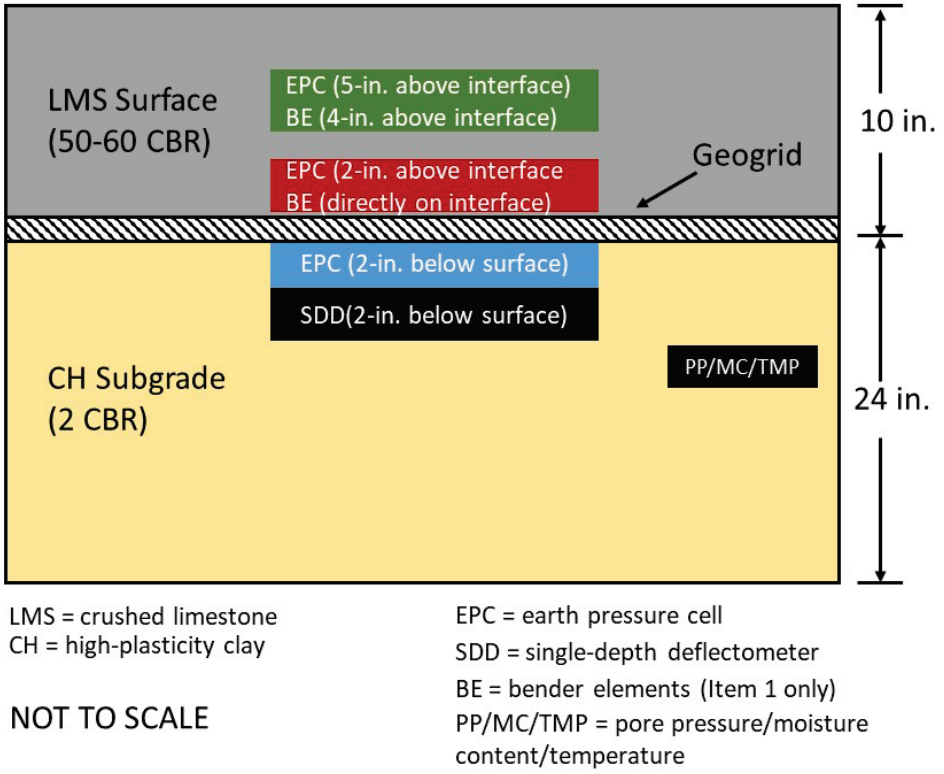

Installation commenced by locating each subgrade EPC at the pre-planned station within each test item and carefully outlining the excavation area to minimize disturbance to adjacent soils. Measurements were made by using a rod and level to determine pre-excavation elevation and to benchmark proper placement depth. The EPC area was excavated to the target depth, the bottom of the excavation was carefully leveled, and a thin layer of clean sand was evenly spread to ensure the gauge maintained full contact with the underlying subgrade soils. Shallow trenches (approximately 1 in. deep) were excavated to the edge of each test item for wire placement and protection from subsequent construction activities. After excavation was complete, an EPC was placed in the excavation, and alignment was verified. Design subgrade soils were placed around each EPC and were compacted in an attempt to minimize density variations in the disturbed area.

Because the base-course EPCs were located near the bottom and mid-depth of the base layer, they were installed prior to final base-course placement. This eliminated the need to excavate a substantial depth of base-course material to facilitate EPC installation, minimized the

probability of aggregate segregation, and mitigated compaction differentials in the area of the EPCs.

Similar to subgrade EPC installation, each base-course EPC was located at the pre-planned location within each test item, existing surface elevation was measured using rod and level techniques, and target EPC placement elevation was determined. Base-course material was hand-placed such that a stable platform was established at the proper finished elevation, i.e. 2 in. or 5 in. above the subgrade surface. Base-course material was placed in relatively thin lifts and compacted using a hand tamper until a stable platform was established. Aggregate fines were used to fill voids in the compacted aggregate platform, to level the gauge, and to ensure the gauge maintained full contact with the underlying surface. Base-course material was placed over and around the gauge and hand-tamped in place to ensure the gauge remained in alignment during subsequent aggregate placement. Completed base EPC installation is shown in Figure 11.

Figure 10. Subgrade EPC installation technique.

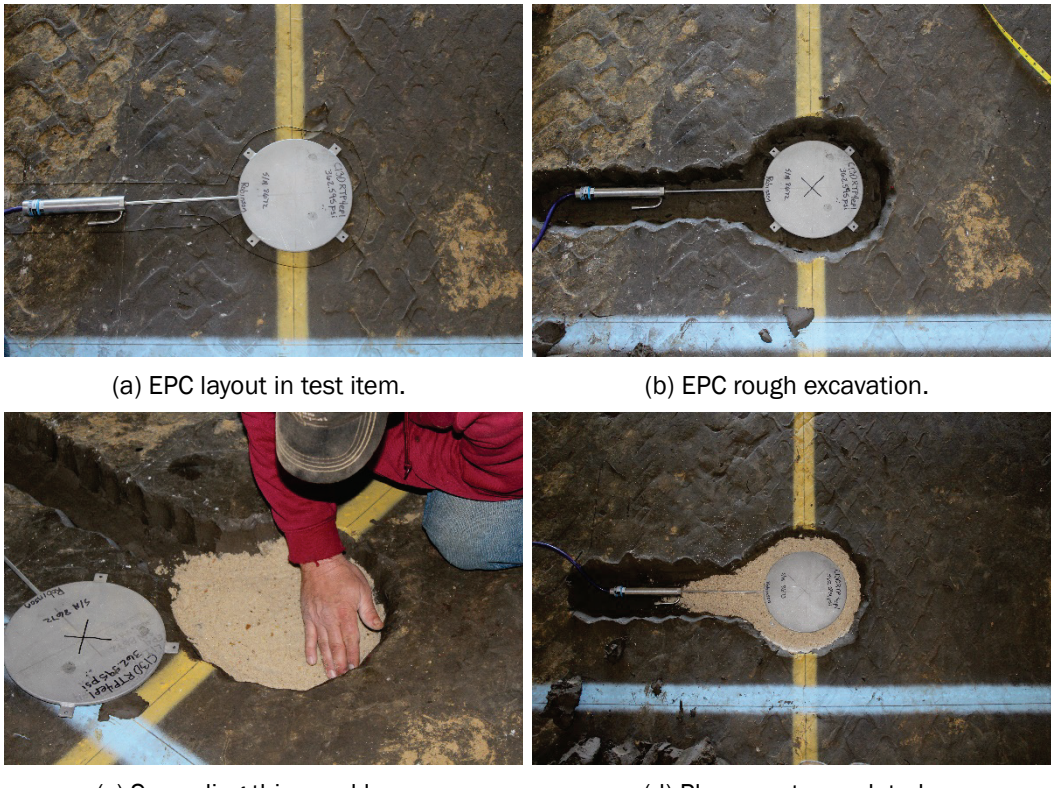

(a) EPC layout in test item. (b) EPC rough excavation.

(c) Spreading thin sand layer. (d) Placement completed.

Figure 11. Base EPC installation prior to base aggregate placement.

4.2 Single-depth deflectometer

Vertical deflections in the subgrade were measured using single-depth deflectometers (SDDs) that were assembled by ERDC. One SDD was placed in the middle of each test item along the centerline of traffic. The SDD was placed such that the shaft was anchored at a depth of 8 ft from the top of the subgrade. A linear velocity displacement transducer (LVDT) with a range of ±1 in. was placed in the housing such that it was in contact with both the anchor rod and the surface plate, as shown in Figure 12. Thus, the LVDT measured movement of the plate 2 in. below the base-subgrade interface relative to the control point located at a depth of 8 ft.

Similar to EPC installation, each SDD was located at a pre-planned location and excavated such that the top of the removable access plate was 2 in. below the existing subgrade elevation. A borehole was advanced at the center of the plate location to a depth of approximately 8 ft by using earth auger drilling techniques. Rapid-setting concrete was placed in the borehole, and the instrument assembly was lowered to the target depth. After the concrete had sufficiently cured, the LVDT was installed through a re-movable access plate such that the tip of the LVDT was in contact with the fixed anchor rod. Subgrade soils were then compacted over the surface of the SDD assembly. Photographs summarizing SDD installation are shown in Figure 13.

Figure 12. Single-depth deflectometer schematic.

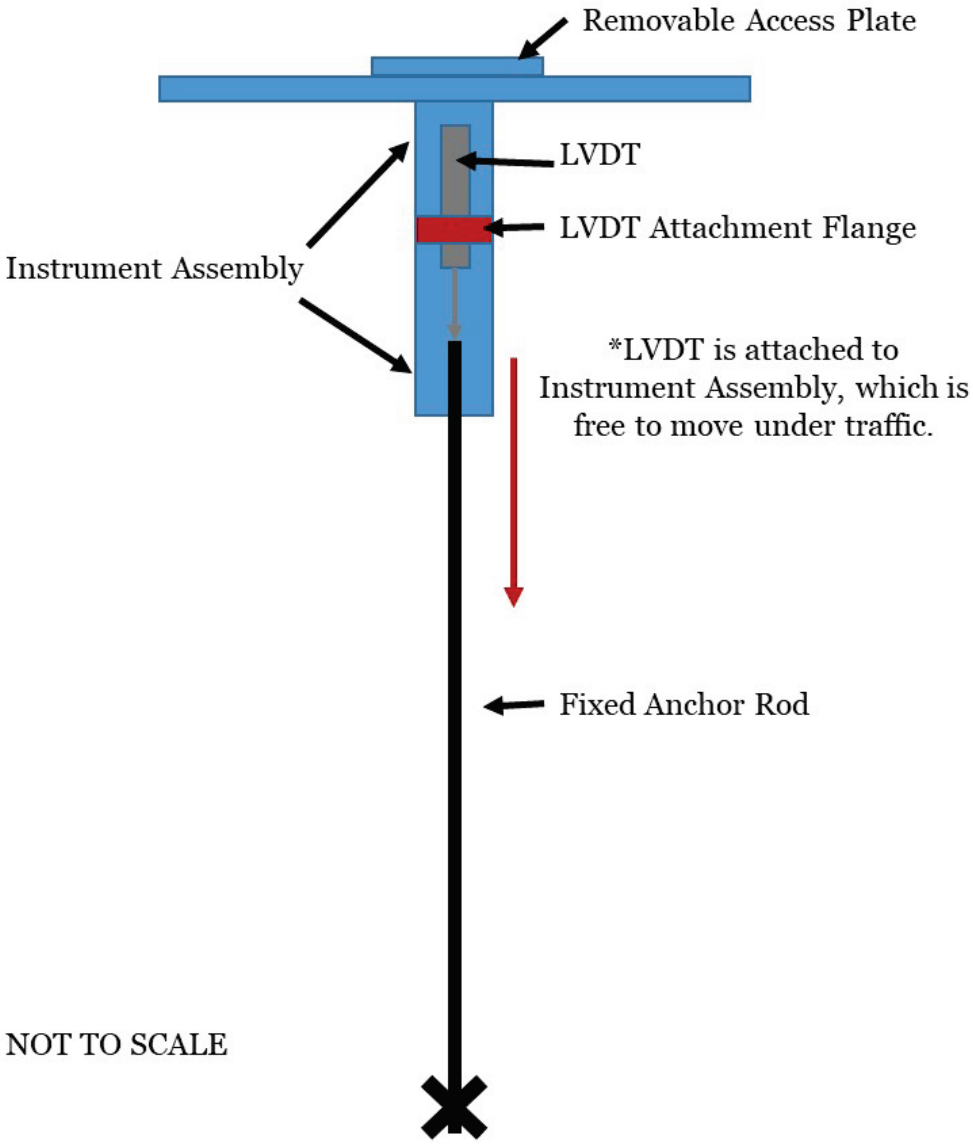

Figure 13. Single-depth deflectometer installation.

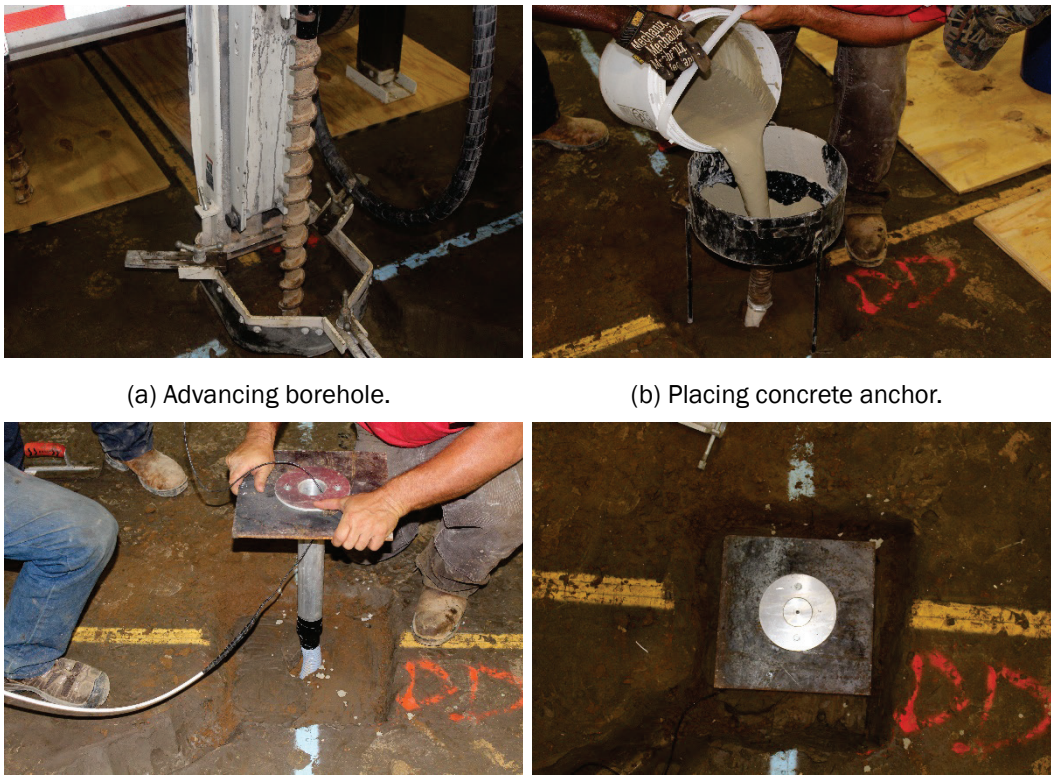

(a) Advancing borehole. (b) Placing concrete anchor.

(c) Setting gauge assembly. (d) Completed installation.

4.3 Bender elements

Shear-wave velocity measurements were made using a set of shear-wave transducers, i.e., bender elements, to identify stiffness changes in the aggregate layer that could be attributed to geosynthetic inclusion. The bender elements were manufactured by the University of Illinois and consisted of a pair of piezoceramic layers bonded to a thin metal shim. Voltage is applied to an element (sender), causing one layer to expand and the other to contract, generating a shear wave. This shear wave is transmitted through the aggregate layer to the opposite element (receiver).

The measurement system consists of a linear amplifier, a signal generator, an oscilloscope, and a filter/amplifier. A signal generator produces an input signal with a magnitude up to 10 V that is delivered to the amplifier where the signal is intensified approximately 6-fold. The shear waves then propagate through the aggregate layer and are recorded by the receiver element. Signal output is filtered/amplified, displayed on the oscilloscope, and saved for further analysis.

The recorded shear-wave signals can be used to calculate shear-wave velocities as follows.

$$V_S = \frac{t_{tip-tip}}{L}$$

where

$t_{tip\text{-}tip}$ = first arrival time
L = distance between the two BE sensors.

Shear modulus of the layer (G_{max}) can then be calculated using the equation

$$G_{max} = pV_S{}^2$$

where

p = bulk density of the aggregate material
V_S = shear-wave velocity.

Elastic modulus (E_{BE}) of the layer can then be calculated using the equation

$$E_{BE} = 2 * \frac{G_{max}}{1 + \nu}$$

where

G_{max} = shear modulus of the aggregate material
ν = Poisson's ratio of the material

Bender element assemblies were placed at two locations in Item 1 that contained NX950. The assemblies were positioned such that the centerline of each assembly, i.e., mid-span, was located along the centerline of the traffic area. Aggregate material was initially placed along the corners of each assembly and at the element housings to ensure alignment was maintained. The entire assembly was then covered with aggregate and hand-tamped to protect the assembly during subsequent aggregate placement. Figure 14 shows the bender element installation.

Figure 14. Bender element installation.

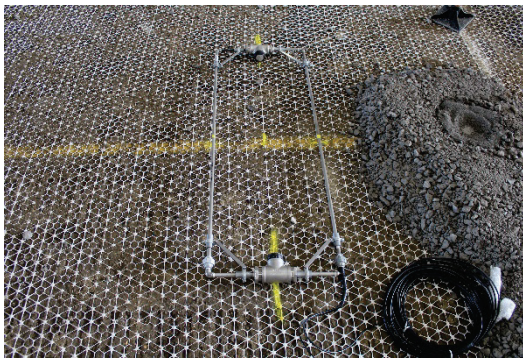

(a) Bender element assembly on geogrid.

(b) Hand-placing aggregate cover.

(c) Completed installation.

4.4 Uniaxial strain gauges

Uniaxial strain gauges were installed on each prototype geogrid to monitor tensile forces developed under test section trafficking and to provide a qualitative comparison between each geogrid product. Twelve strain gauges were installed on each geogrid (Table 2); six locations were selected, and strain gauges were installed on both the top and bottom of the geogrid at each location. Locations were selected such that gauges were installed along the centerline of traffic and offset approximately 17 in. to either side of centerline, i.e., corresponding to the edge of the proposed wander pattern. Thus, gauge response could be used to understand strains developed along the assumed rut depth basin.

Two types of strain gauges were installed, i.e., Micro-Vishay model EP-08-125-350 (UXEP) and Micro-Vishay CEA-06-125-350 (UXCEA). Differing strain gauge types were installed as a means to monitor gauge installation techniques and survivability to aid in the selection of the most appropriate gauge type for future consideration. UXEP had a high-elongation polyimide backing with a range of 10% of the gauge length. UXCEA was a grid encapsulated gauge with copper solder tabs and a range of 3% of the gauge

length. All gauges were located at the nodes of each prototype geogrid to provide sufficient installation area to promote gauge survivability.

Surface preparation began by milling down the node to match the thickness of the surrounding ribs, thus providing a flat surface and minimizing gauge curvature. After milling the node locations, it was observed that the milled surface was softer than the pre-existing outer layer, attributed to the composite or layering technique used to manufacture these particular geogrids, and that the gauges did not adhere to the node using traditional techniques, i.e., M-Bond 200. Thus, a thin layer of M-Bond AE-10 was applied to each location, allowed to completely cure, and sanded with emery cloth to promote gauge adhesion using M-Bond 200.

The test grids were unrolled and thick cardboard was placed under each gauge location to protect the grid during gauge preparation and installation as previously described. After all gauges were installed on one side of a geogrid, Teflon sheets were taped over the gauge location to protect the installed gauges such that gauges could be adhered to the opposite side of the geogrid. Similarly, cardboard was used to protect the geogrid and previously installed gauges.

After all gauges were installed on both sides of the geogrid, the rolls were stood up on end, unrolled, and suspended vertically to facilitate data cable installation. The gauges and tabs were wired by soldering them together ensuring wire strain relief was provided between them. After soldering was complete, the wires were cleaned with acetone or alcohol, and Gagekote #8 was applied as a moisture block. Finally, Dow Corning 3145 RTV adhesive/sealant was applied as a waterproofing over all strain gauges, wire terminals, and lead wires.

After all gauges had been encapsulated in waterproofing sealant, a temporary wooden frame was secured at each location to protect the installed gauges from bending when rolling/unrolling the geogrid in the test section. Once the geogrids were unrolled at the designated location in each test item, the wooden frames were carefully removed.

A layer of aggregate fines was placed over the strain gauges to provide protection during aggregate placement. Aggregate base was placed over each location and hand-tamped in place prior to subsequent aggregate placement (Figure 15).

Figure 15. Uniaxial strain gauge protection during placement.

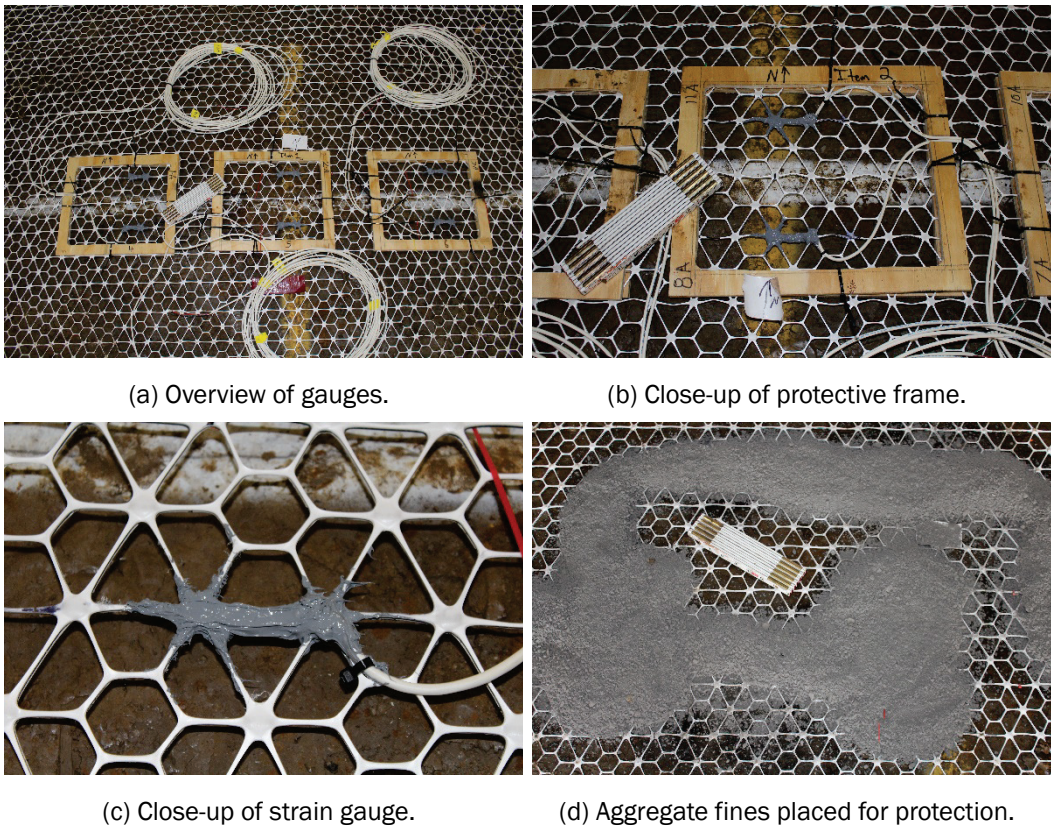

(a) Overview of gauges.

(b) Close-up of protective frame.

(c) Close-up of strain gauge.

(d) Aggregate fines placed for protection.

Table 2. Uniaxial strain gauge identification.

Location	Gauge Type	Gauge Designation	Surface	Transverse Offset (in.)[1]
Item 1 (NX950)	EP-08-125- 350	1A	Top	17.75 (W)
Item 1 (NX950)	EP-08-125- 350	1B	Bottom	17.75 (W)
Item 1 (NX950)	EP-08-125- 350	2A	Top	0
Item 1 (NX950)	EP-08-125- 350	2B	Bottom	0
Item 1 (NX950)	EP-08-125- 350	3A	Top	17.75 (E)
Item 1 (NX950)	EP-08-125- 350	3B	Bottom	17.75 (E)
Item 1 (NX950)	CEA-06-125-350	4A	Top	17.75 (W)
Item 1 (NX950)	CEA-06-125-350	4B	Bottom	17.75 (W)
Item 1 (NX950)	CEA-06-125-350	5A	Top	0
Item 1 (NX950)	CEA-06-125-350	5B	Bottom	0
Item 1 (NX950)	CEA-06-125-350	6A	Top	17.75 (E)
Item 1 (NX950)	CEA-06-125-350	6B	Bottom	17.75 (E)
Item 2 (NX750)	EP-08-125- 350	7A	Top	16.25 (W)
Item 2 (NX750)	EP-08-125- 350	7B	Bottom	16.25 (W)
Item 2 (NX750)	EP-08-125- 350	8A	Top	0
Item 2 (NX750)	EP-08-125- 350	8B	Bottom	0
Item 2 (NX750)	EP-08-125- 350	9A	Top	16.5 (E)
Item 2 (NX750)	EP-08-125- 350	9B	Bottom	16.5 (E)
Item 2 (NX750)	CEA-06-125-350	10A	Top	16.25 (W)
Item 2 (NX750)	CEA-06-125-350	10B	Bottom	16.25 (W)
Item 2 (NX750)	CEA-06-125-350	11A	Top	0
Item 2 (NX750)	CEA-06-125-350	11B	Bottom	0
Item 2 (NX750)	CEA-06-125-350	12A	Top	16.5 (E)
Item 2 (NX750)	CEA-06-125-350	12C	Bottom	16.5 (E)

[1]Transvere offset was measured East (E)/West (W) of centerline.

5 Pavement Characterization

5.1 As-built properties

Quality-control tests were performed during construction of each material lift to ensure target values were achieved and to monitor material consistency. Dry density and moisture content were measured using a nuclear moisture density device in accordance with ASTM D6938 (2017b) to verify the uniformity of each material lift. Field in-place CBR tests were performed in general accordance with ASTM D4429 (2009) on each compacted lift to ensure target values were achieved. To further characterize the strength of the completed aggregate surface and subgrade layers, Dynamic Cone Penetrometer (DCP) tests were performed in accordance with ASTM D6951 (2018). As-built properties are summarized in Table 3.

As-built properties should be evaluated to identify potential differences in test item construction that could influence performance outcomes. A review of key subgrade construction characteristics suggest that the three test items had similar properties. Average dry density ranged from 82.3 to 83.5 pcf, and Item 1 had a slightly higher density than the other test items. Average oven-dried moisture contents, as well as CBR, were nearly identical for all test items, suggesting that any observed performance differences could be attributed to geosynthetic inclusion rather than differences in subgrade construction.

A review of aggregate surface properties indicated that dry density was the highest in Item 1, which contained NX950; followed by Item 2, which contained NX750; and, finally, the unstabilized control. This may suggest that NX950, which had the largest rib width and rib height, improved compactability of the aggregate layer, as all test items received the same level of compactive effort at the same time. Compaction in Item 1 was 95.7% of modified Proctor, and Item 2 and Item 3 were generally 93% of modified Proctor. Differences in final average compacted thickness of the aggregate layer were slightly over 0.5 in. but were considered acceptable. Recall the aggregate layer contained up to 1-in. maximum aggregate size material; thus, it was attempted to limit variances in aggregate layer thickness to ½ the maximum aggregate size, or in this case, 0.5 in. The unstabilized item, i.e., Item 3, had the thickest average aggregate layer (10.9 in.) when compared to Item 1 (10.3 in.) and Item 2 (10.7 in.).

Average aggregate CBR values were approximately 50, and it is noted that this material type typically yields CBRs on the order of 80-100 when placed in multiple 6- to 8-in. lifts. However, due to the weakness of the subgrade, the aggregate layer was placed in one single lift, simulating a typical construction practice of bridging over soft material to reduce subgrade pumping. Notably, variability, i.e., standard deviation, in the measured values was lowest in Item 1 that contained NX950. Item 3 had the most variability, suggesting that the geogrids improved the uniformity of the measured CBR values, which tend to agree with compaction observations.

Table 3. Summary of as-built properties.

Property	Item 1 (NX950)	Item 2 (NX750)	Item 3 (Unstabilized)
CH Subgrade (MDD =106.1 pcf @ OMC = 17.1%)[1]			
Wet Density (pcf)	112.2 ± 1.6	112.2 ± 1.9	111.9 ± 1.4
Dry Density (pcf)	83.5 ± 2.0	82.6 ± 2.7	82.3 ± 1.9
Nuclear Moisture Content (%)	33.8 ± 2.6	36.5 ± 3.2	37.2 ± 3.1
Compaction (%)	78.7	77.9	77.6
Oven-Dried Moisture (%)	40.4 ± 1.6	40.7 ± 1.5	40.6 ± 1.6
In-Place CBR (%)	2.0 ± 0.3	2.0 ± 0.3	2.1 ± 0.3
Aggregate Surface (MDD = 147.9 pcf @ OMC = 5.2%)[1]			
Wet Density (pcf)	147.6 ± 1.9	143.5 ± 2.0	142.6 ± 2.7
Dry Density (pcf)	141.5 ± 1.9	138.3 ± 1.7	137.5 ± 2.5
Nuclear Moisture Content (%)	4.3 ± 0.4	3.8 ± 0.2	3.7 ± 0.3
Compaction (%)	95.7	93.5	93.0
Oven-Dried Moisture (%)	2.9 ± 0.2	2.8 ± 0.3	3.2 ± 0.4
In-Place CBR (%)	52.0 ± 3.0	47.3 ± 5.3	52.3 ± 11.8
Thickness (in.)	10.3 ± 0.4	10.7 ± 0.2	10.9 ± 0.2

[1]Maximum dry density and optimum moisture content as determined from ASTM D1557; MDD = maximum dry density; OMC = optimum moisture content; CBR = California bearing ratio

5.2 Falling weight deflectometer

Falling weight deflectometer (FWD) tests were performed on the surface of the test items after construction and prior to trafficking. The measured impulse stiffness modulus (ISM) was used to evaluate the stiffness of the constructed pavement section and to provide a baseline for subsequent comparison under traffic. The ISM is the ratio of the applied load to the measured plate deflection with higher values representing a stiffer pavement structure. Initial ISM, i.e., pre-traffic, values are summarized in Table 4. The

values represent an average of five test locations each in Item 1 and Item 2 and four test locations in Item 3. A slightly higher initial ISM was measured in Item 1 and 2 when compared to Item 3. As-built properties suggested that Item 3 should be slightly stiffer than Item 1 and Item 2, i.e., slightly higher subgrade CBR and thicker aggregate layer; thus, it is hypothesized that the geogrids provided some initial stiffness improvement.

Table 4. Initial average ISM measurements.

Location	Load (lb)*	Plate deflection (mils)*	ISM (kips/in.)
Item 1 (NX950)	8930	82.38	108
Item 2 (NX750)	8906	81.95	109
Item 3 (Unstabilized)	8773	84.35	104

ISM = impulse stiffness modulus; *values represent average of third drop measurements

6 Traffic Testing

Simulated truck traffic was applied by using a single-axle dual-wheel tire configuration mounted to a steel frame that was capable of being loaded with a series of cast lead weights to achieve the targeted total load. The loaded steel frame was mobilized via a military truck. The steel frame was outfitted with outrigger tires on each side, near the mid-span of the load frame, as a means of stabilizing the frame and preventing overturn. During traffic application, one outrigger remained in contact with the pavement to ensure overall stability. The opposite outrigger was elevated such that it was not in contact with the pavement surface but was near the surface in case of an overturn condition.

The load cart (Figure 16) was outfitted with a single-axle dual-wheel truck gear that was loaded with cast lead weights to target a 10,000-lb total gear load, i.e. 5,000 lb per tire total load. Tire inflation pressure was maintained at 120 psi throughout testing.

Figure 16. Load cart for simulated traffic.

a) Overall view of load cart. b) Close-up of dual wheel truck gear.

Prior to initial traffic application, tire imprints were obtained to measure tire contact area at differing test loads and tire pressures. The imprints were made by affixing a thick construction paper outline to a thin rubber membrane that was placed on the aggregate surface. The loaded test tire was rolled onto the paper outline, and the area around each tire was painted using marking paint. The marking paint was allowed time to dry such that, when the tire was reversed off the paper outline, a distinguishable paint halo was preserved. Each tire imprint was photographed and uploaded to a computer-aided drawing program to aid in measuring tire contact dimensions. Measurement results are

summarized in Table 5. Total area is simply the area inside the outline of the tires, where contact area excludes the tire treads.

It was found that the right tire, i.e., the tire closer to the outrigger tire, had a larger contact area than the left tire in all loading conditions. It is believed that this was attributed to a slight tilt in the load cart towards the outrigger, which prevents overturn, thus increasing the load on the right tire. In general, it was found that an increase in tire pressure decreased contact area, and conversely, an increase in load increased contact area. Notably, a set of tire prints were collected with the test tire located on a concrete surface, and it was found that tire contact area decreased when compared to the same loading condition on the aggregate surface. This suggests that, at least in a static condition, the pavement surface type can influence the measured tire contact area, and that a flexible surface can result in a higher contact area than a rigid surface.

Table 5. Measured test tire dimensions.

Load (lb)	Inflation Pressure (psi)	Left Tire Area (in.^{2})	Right Tire Area (in.^{2})	Total Area (in.^{2})	Contact Area (in.^{2})
Empty (6,675)	100	54.3	65.4	119.7	99.2
Empty (6,675	120	50.6	63.3	113.9	94.9
Full (10,375)	100	66.6	78.5	145.1	122.0
Full (10,375)	120	60.1	76.9	137.0	116.0
Full (10,375)[1]	120	55.6	67.3	122.0	105.5

[1]Measurement made on a concrete surface

A normally distributed traffic pattern (Figure 17) with a total wander width of approximately 36 in. was used to apply test traffic to each test item. Traffic was applied bi-directionally, where one pass was advanced forward in the selected position, and the return pass was applied in the same selected position. Tire position was maneuvered in the buffer zone areas to minimize effects from side shifting the load frame within the test area. Testing speed was approximately 2.7 mph.

Figure 17. Normally distributed traffic pattern.

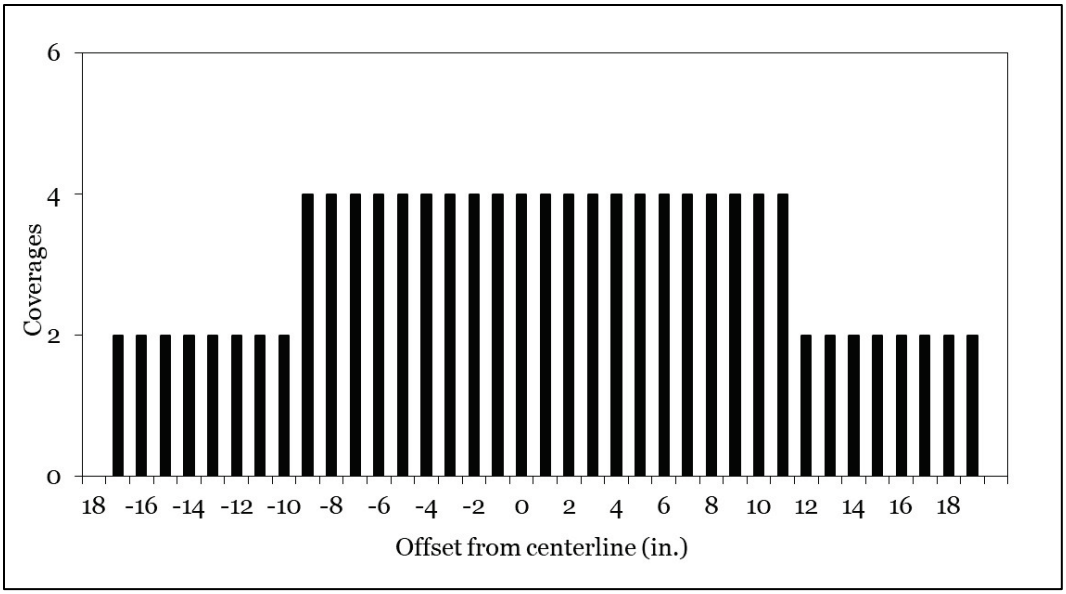

7 Results

Failure of the unsurfaced test items was targeted as 3 in. of rutting, where rutting included permanent surface deformation in the wheel path and upheaval outside the wheel path (Figure 18), or 10,000 traffic passes, whichever occurred first. Instrumentation response data and falling weight data were gathered at selected traffic intervals to facilitate pairwise comparison of test item performance.

Figure 18. Example of rut depth and permanent deformation measurement.

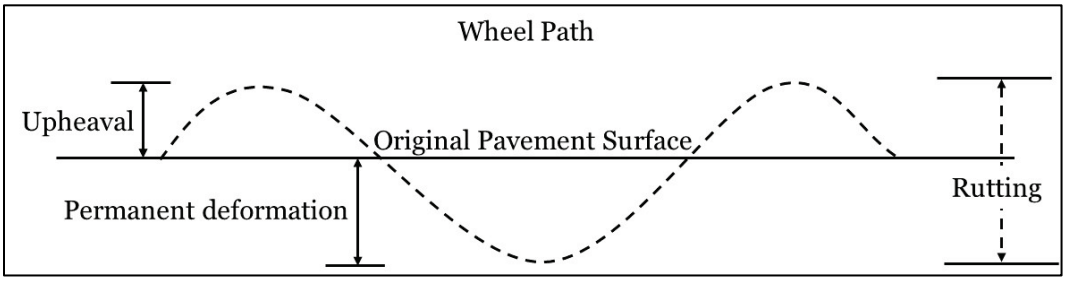

Results are presented for each measured performance metric, and comparisons are made based on identified trends with traffic application. Further, a statistical analysis of each performance metric was performed to determine if observed differences were statistically significant. A paired t-test was considered appropriate because all test data were collected at the same traffic interval, and construction techniques were identical for each test item. A paired t-test assumes that the dependent variable, i.e., the difference in observed performance is continuous, the measurements are independent, the dependent variable is normally distributed, and the dependent variable does not contain any outliers. For the statistical analysis, a two-tailed rejection region was considered, i.e., the average difference between the observed values was zero, and all statistical measures were evaluated at $\alpha = 0.05$.

7.1 Surface deformation

Rutting measurements were made using a 12-ft-long aluminum straightedge and a machined depth wedge, and permanent surface deformation measurements were made using a Trimble robotic total station.

Rut depth progression is presented in Figure 19. Rutting performance was generally equivalent up to approximately 400 passes, i.e., about 0.25 in. rutting, suggesting that there was a period of initial shakedown or

densification in the aggregate layer. After approximately 400 passes, it was observed that rutting performance began to diverge. Item 1 had the best rutting performance and contained NX950. Item 2 was the next best performer and contained NX750. Rutting performance improvement in Item 1 could be attributed to the larger rib width and rib height of NX950. Item 3 was the worst performer, as expected, and had approximately 0.5 in. more rutting at 2,000 passes. At the completion of trafficking, Item 3 had 1.8 in. more rutting than Item 1 and 1.4 in. more rutting than Item 2. Thus, the inclusion of geogrids dramatically improved rutting performance under the conditions of this study. Photographs highlighting rut depth progression at select traffic intervals are shown in Figures 20 through 22.

Figure 19. Rut depth progression with traffic.

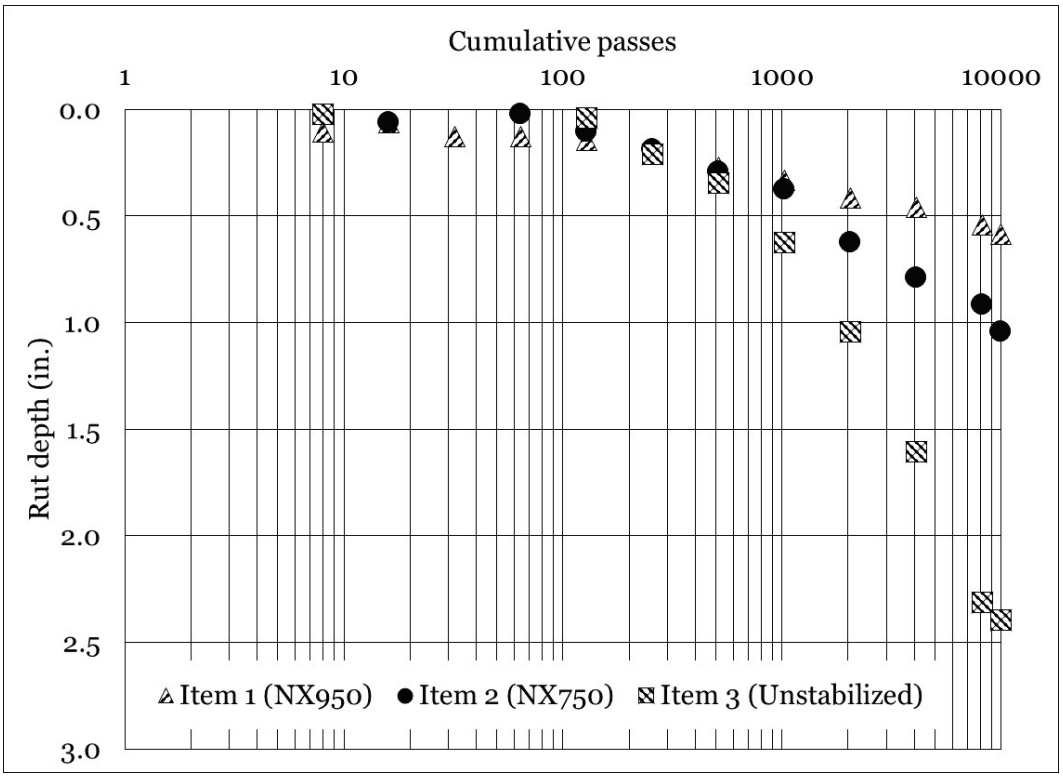

Figure 20. Rut depth progression in Item 1 (NX950).

(a) Pass 512.

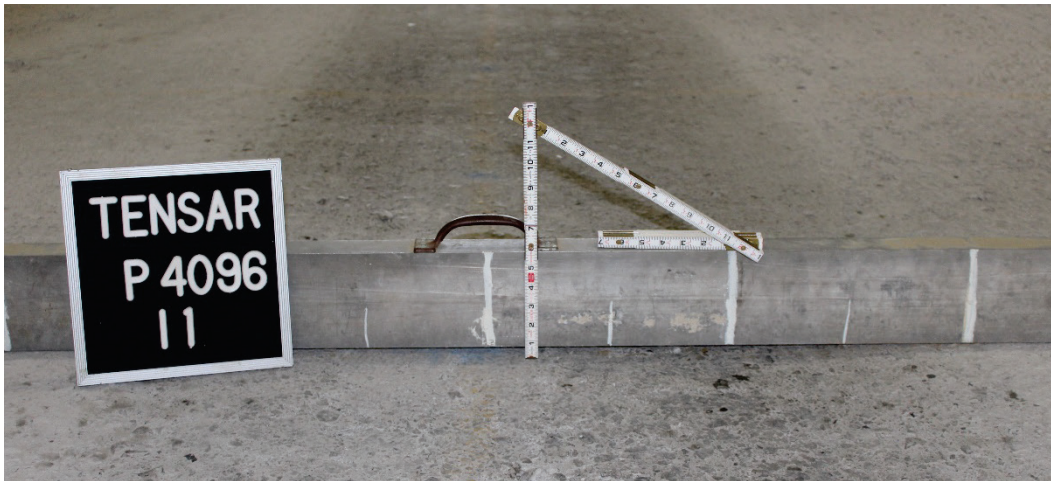

(b) Pass 4,096.

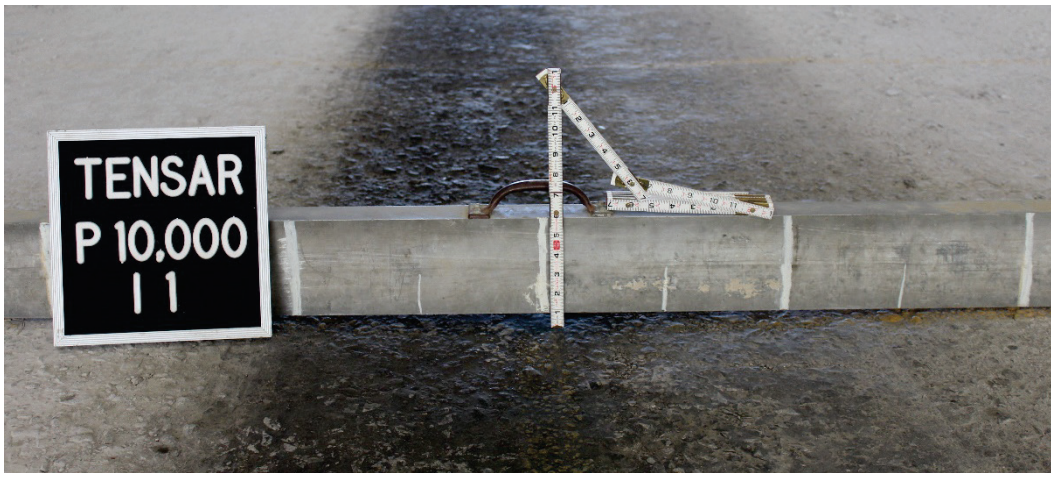

(c) Pass 10,000.

Figure 21. Rut depth progression in Item 2 (NX750).

(a) Pass 512.

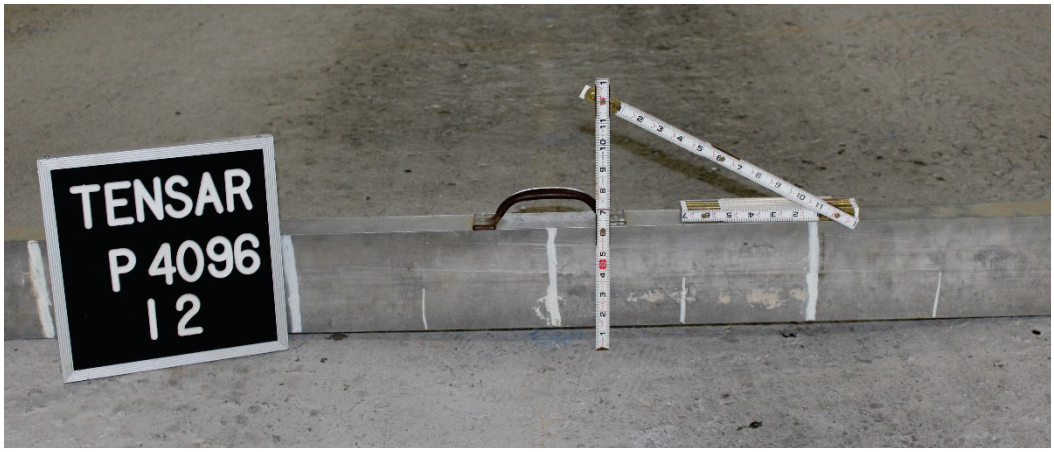

(b) Pass 4,096.

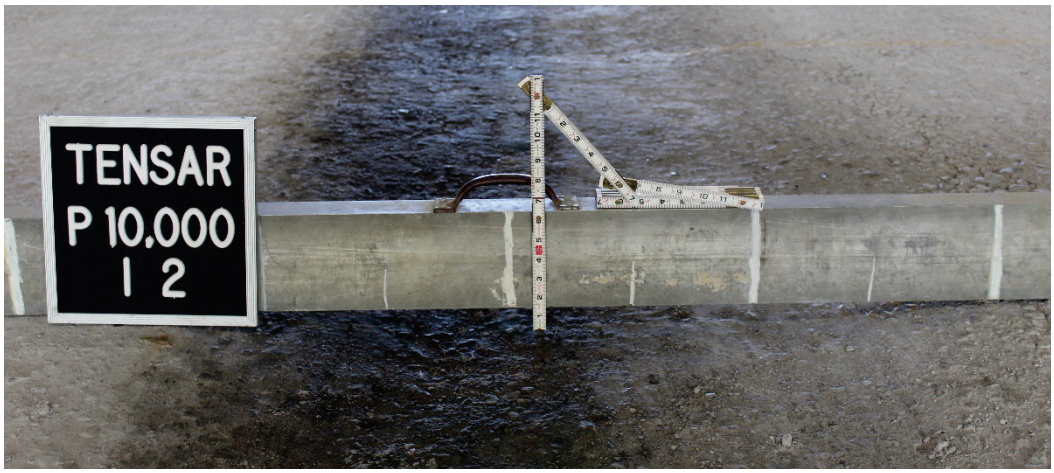

(c) Pass 10,000.

Figure 22. Rut depth progression in Item 3 (unstabilized).

(a) Pass 512.

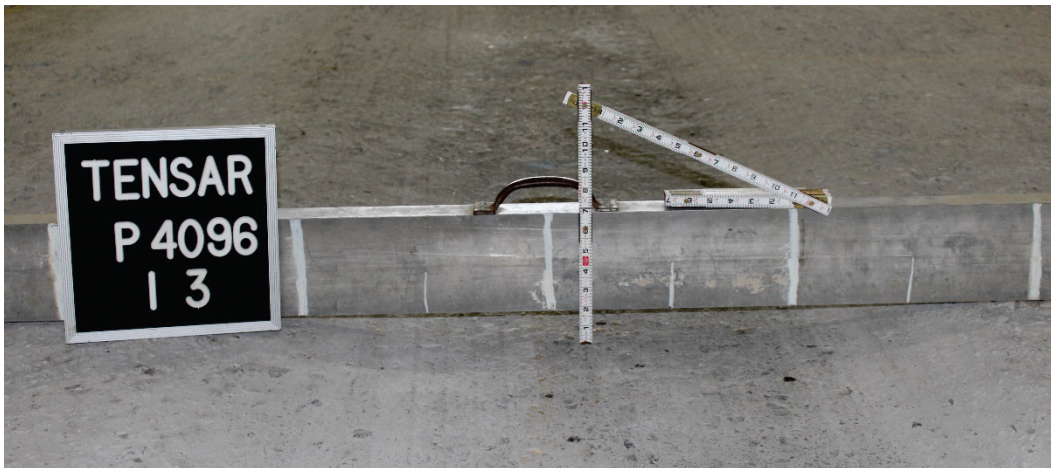

(b) Pass 4,096.

(c) Pass 10,000.

A paired t-test indicated that none of the interactions was statistically significant, which was an unexpected result. However, a review of the data showed that very little rutting occurred early in traffic, i.e., up to 128 passes, after which rutting began to develop. Thus, the differences at early data collection points were near zero introducing bias in the statistical measure. When the analysis was conducted on data points after 128 passes, meaningful and expected statistical differences were observed (Table 6). The analysis indicated that all comparisons were statistically significant, and that average rutting in Item 3 (unstabilized) was more than average rutting in Item 1 (NX950) and Item 2 (NX750). Further, Item 1 (NX950) was found to be statistically different from Item 2 (NX750), and average rutting performance was found to be better in Item 1 (NX950).

Table 6. Statistical analysis – rut depth.

Interaction	n	p-value	Significant	Better Performer
Item 1 vs. Item 2	8	0.043	Yes	Item 1
Item 1 vs. Item 3	8	0.039	Yes	Item 1
Item 2 vs. Item 3	8	0.039	Yes	Item 2

Permanent surface deformation with traffic is presented in Figure 23. Comparable to rutting performance, generally similar behavior was observed up to 400 passes. Differences in permanent deformation became evident after 400 passes, and Item 3 (unstabilized) had more permanent deformation than Item 1 (NX950) and Item 2 (NX750). The difference in measured rut depth and permanent deformation gives an indication of the amount of aggregate upheaval, i.e., shear flow, occurring in the aggregate layer. It was observed that the test items containing geogrids had little measured upheaval outside the wheel path, suggesting that the geogrids improved the overall stability of the aggregate layer. Item 3 (unstabilized) had a meaningful amount of upheaval outside the wheel path, i.e., approximately 0.8 in. at the completion of trafficking. Noteworthy depressions were observed at the transition onto/off Item 3 (unstabilized) as shown in Figure 24. It is hypothesized that as the rolling test wheel moved off the more stable geogrid test item, a dynamic loading condition existed that increased deformation in these areas. At times, the depressions became of sufficient depth that repairs were required. The areas were simply filled with native limestone aggregate such that traffic could continue. It is noted that the depressions were outside measurement locations, i.e., cross sections, and did not influence rut depth measurements.

Figure 23. Permanent deformation with traffic.

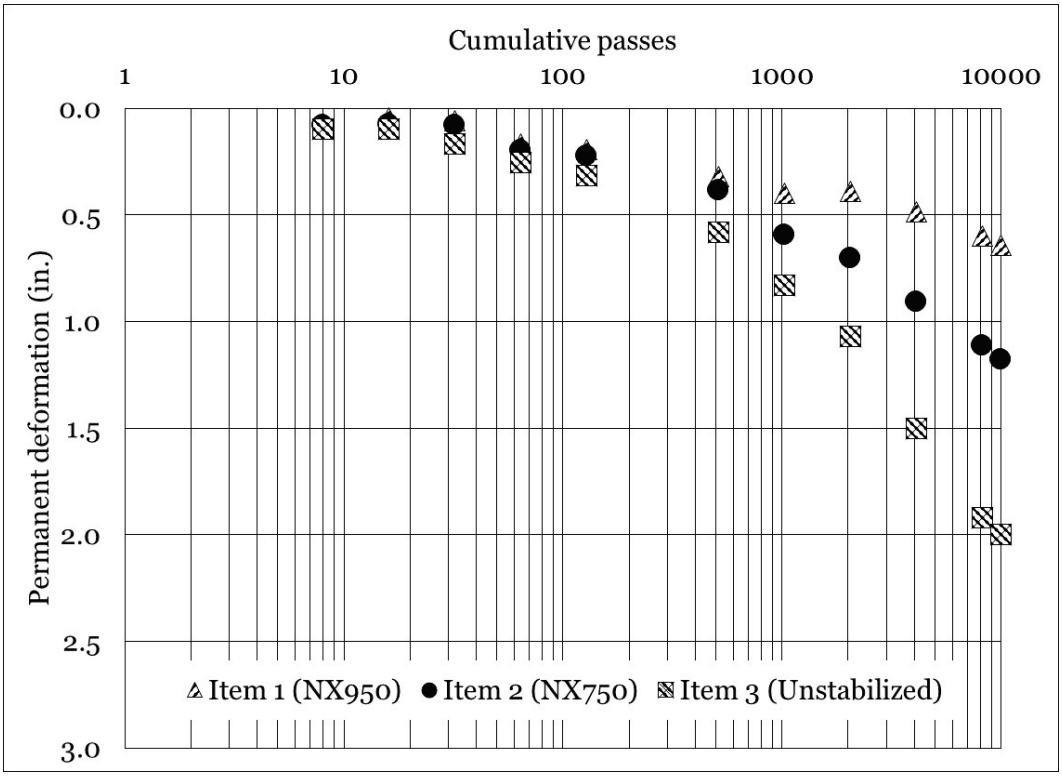

Figure 24. Depression at transition from Item 2 (NX750) to Item 3 (unstabilized).

The results of a statistical analysis for permanent surface deformation are presented in Table 7. All comparisons were found to be statistically

significant, indicating that average permanent deformation was different in all test items. Item 1 (NX950) was found to have the lowest average permanent deformation. Item 2 (NX750) was found to be the next best performer, followed by Item 3 (unstabilized).

Table 7. Statistical analysis – permanent surface deformation.

Interaction	n	p-value	Significant	Better Performer
Item 1 vs. Item 2	12	0.010	Yes	Item 1
Item 1 vs. Item 3	12	0.008	Yes	Item 1
Item 2 vs. Item 3	12	0.007	Yes	Item 2

7.2 Impulse stiffness

Falling weight deflectometer (FWD) data were collected at each traffic interval to monitor overall structural deterioration with increasing traffic levels. The Impulse Stiffness Modulus (ISM), which is the applied load divided by the measured plate deflection, was used as the basis for comparison. FWD data were collected at the location of installed instrumentation in each test item. Thus, pavement stiffness and instrumentation response were collected at each FWD test location. Average ISM values for each test item at each traffic interval were calculated and used for analysis. Average ISM values for the traffic duration are presented in Figure 25.

Initial ISM values indicated that Item 1 (NX950) and Item 2 (NX750) were slightly stiffer than Item 3 (unstabilized), which could be an indication of initial stiffening provided by the geogrids. A generally decreasing trend in ISM was observed for all test items with an increase in applied traffic and pavement deterioration. At the 512-pass data collection point, weight had to be removed from the falling weight device to account for over ranging deflection values. This resulted in a notable decrease in calculated ISM. However, in general, it was observed that Item 1 (NX950) had the highest ISM, followed by Item 2 (NX750), and finally Item 3 (unstabilized) over the duration of traffic. This suggests that the geogrids providing a stiffening of the aggregate layer throughout traffic application, which agrees with rutting observations.

A statistical analysis of calculated ISM values is provided in Table 8. Item 1 (NX950) was found to be statistically different from the other two test items and was the better performer in both cases. Differences in Item 2

(NX750) and Item 3 (unstabilized) were unremarkable (p-value = 0.205), indicating that average ISM was equivalent.

Figure 25. Impulse stiffness with traffic.

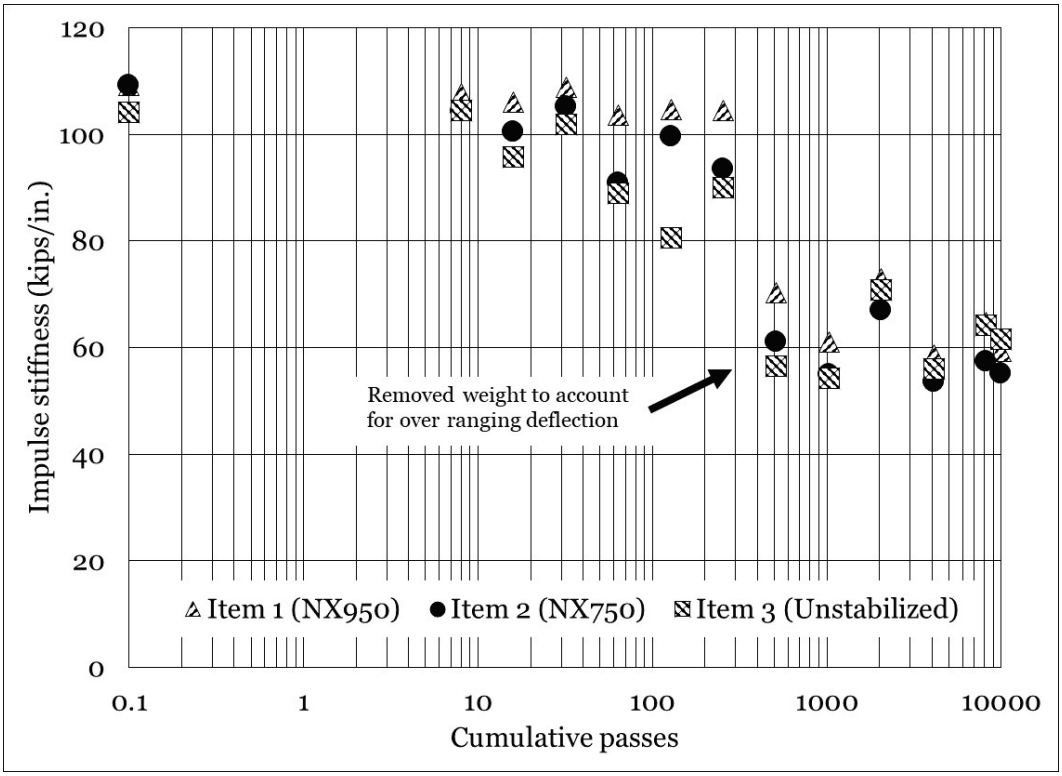

Table 8. Statistical analysis – impulse stiffness modulus.

Interaction	n	p-value	Significant	Better Performer
Item 1 vs. Item 2	13	<0.001	Yes	Item 1
Item 1 vs. Item 3	13	0.001	Yes	Item 1
Item 2 vs. Item 3	13	0.205	No	Same

7.3 Subgrade pressure response

Representative subgrade response values were determined by graphically selecting the highest measured response near the end of each selected traffic interval. Thus, the values selected represent a "best hit," when the test gear was directly over the subgrade EPC. Response values were calculated by subtracting the peak value from the minimum value for the event; thus, values represent dynamic measurements. An example of selecting response values for an EPC are shown in Figure 26. Maximum subgrade pressure response for each test item are presented in Figure 27.

Maximum measured subgrade pressure was relatively consistent over the duration of test traffic, and a slight increase was observed early in traffic, i.e., up to approximately 100 passes. Item 3 (unstabilized) had a marginally higher measured subgrade pressure than Item 1 (NX950), i.e., average 6.8% increase, and Item 2 (NX750), i.e., average 4.9% increase, for a majority of traffic application. A more definitive increase in subgrade pressure in Item 3 (unstabilized), when compared to Item 1 (NX950), i.e., 15.7% increase, and Item 2 (NX750), i.e., 13.9% increase, was observed near the final data collection points. These observations suggest that the geogrids effectively reduced measured pressure on the subgrade, particularly at higher levels of surface deformation.

The results of a statistical analysis of measured subgrade pressure are presented in Table 9. All interactions were found to be statistically significant, indicating that meaningful differences were observed. Item 1 (NX950) was the best performer, having the lowest average subgrade pressure. Both geogrid stabilized items, i.e., Item 1 (NX950) and Item 2 (NX750), had statistically lower average subgrade pressures than the unstabilized Item 3.

Figure 26. Example of peak response selection.

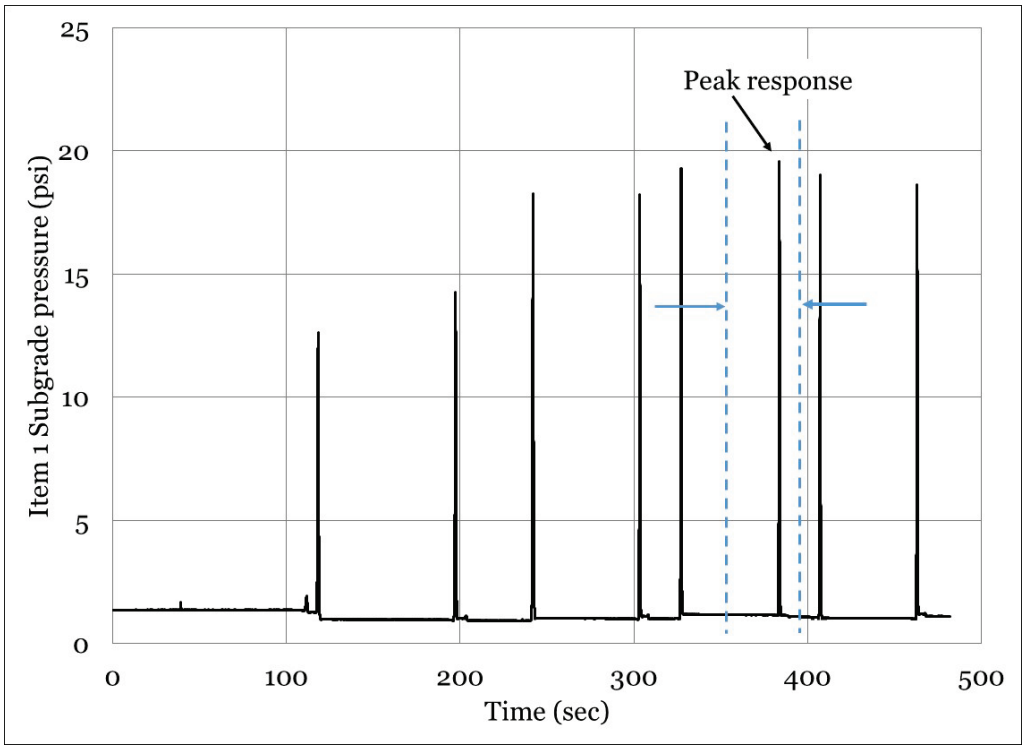

(a) Example of peak selection

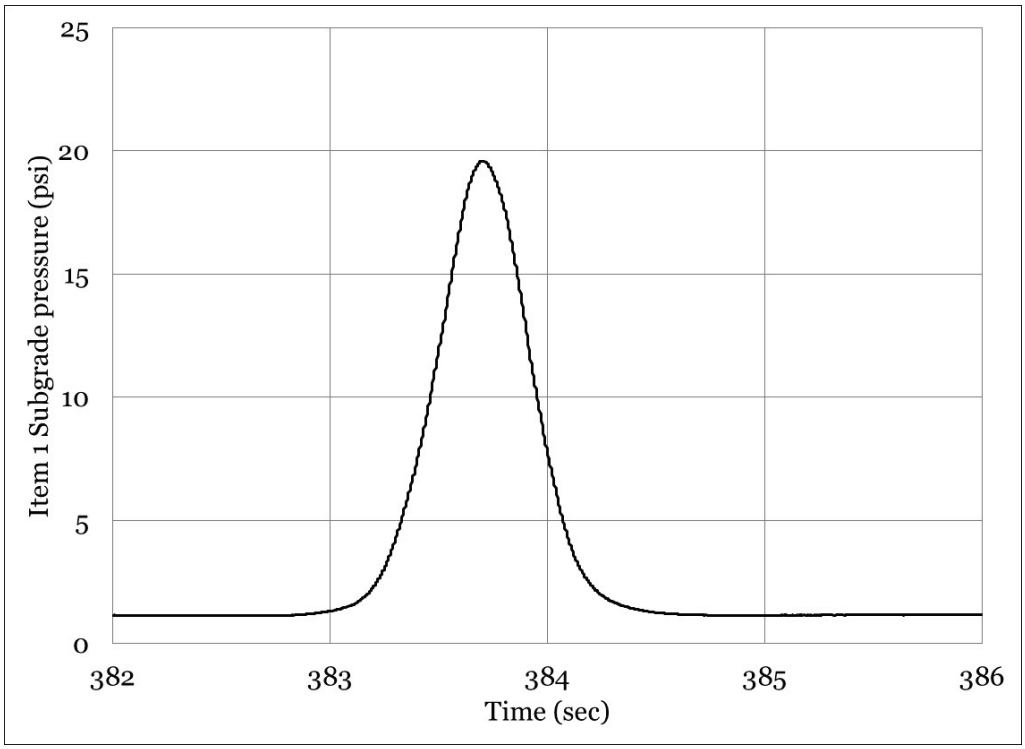

(b) Close-up of selected response

Figure 27. Maximum measured subgrade pressure with traffic.

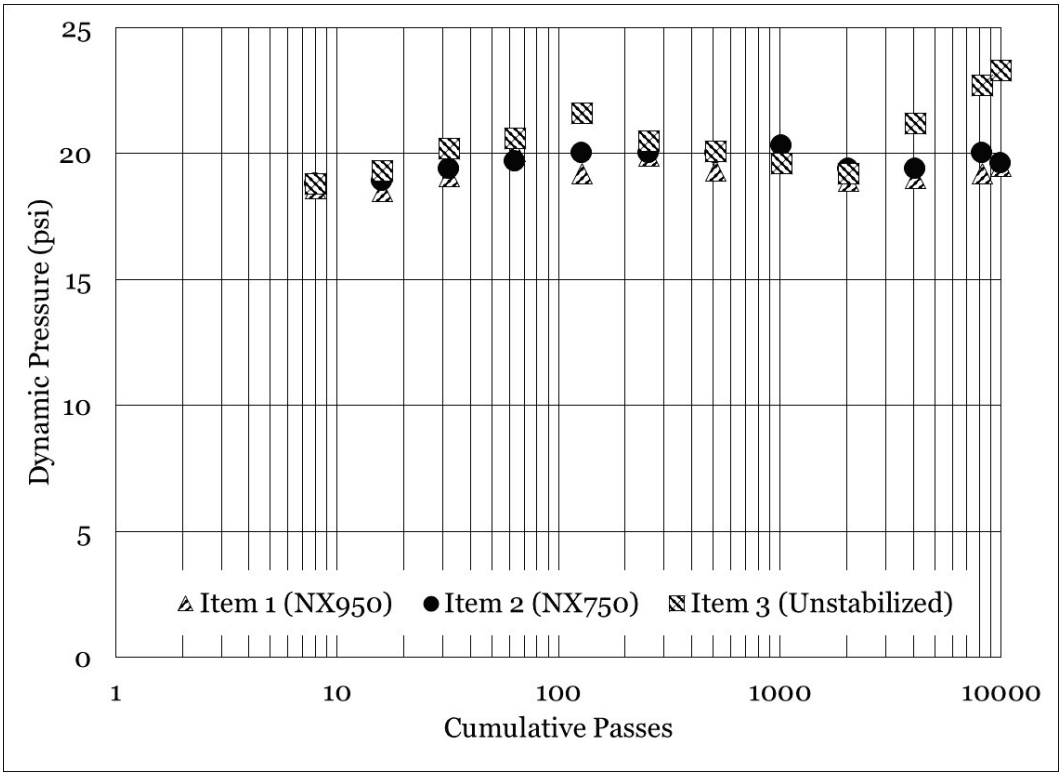

Table 9. Statistical analysis – subgrade pressure response.

Interaction	n	p-value	Significant	Better Performer
Item 1 vs. Item 2	12	0.003	Yes	Item 1
Item 1 vs. Item 3	12	0.004	Yes	Item 1
Item 2 vs. Item 3	12	0.024	Yes	Item 2

7.4 Aggregate pressure response

Representative aggregate pressure response values were selected using the same methodology as that described for subgrade pressure response. The "best hit" was selected, and reported values represent the peak dynamic response measured during a selected traffic interval. Maximum aggregate pressure response measured mid-depth (MD) of the aggregate layer is shown in Figure 28.

Aggregate pressure response at mid-depth of the aggregate layer was found to be generally consistent throughout most of traffic application. Similar to measured subgrade response values, an increase in MD aggregate pressure response was observed at the last two data collection intervals. Higher MD base response values were observed in Item 1 (NX950) when compared to Item 2 (NX750) and Item 3 (unstabilized)

over the duration of traffic application. On average, MD base pressure in Item 1 (NX950) was 15.5% higher than Item 2 (NX750) and 16.9% higher than Item 3 (unstabilized), which may be attributed to stiffening of the aggregate layer from geogrid inclusion. Thus, the stiffened aggregate layer appeared to redistribute applied pressure higher in the pavement structure, which agreed with observed reductions in measured subgrade pressure. Differences in measured values were not as dramatic in Item 2 (NX750) and Item 3 (unstabilized), where the Item 2 (NX750) measured MD aggregate pressure was, on average, 1.7% higher than Item 3 (unstabilized).

Figure 28. Measured maximum aggregate pressure (mid-depth) with traffic.

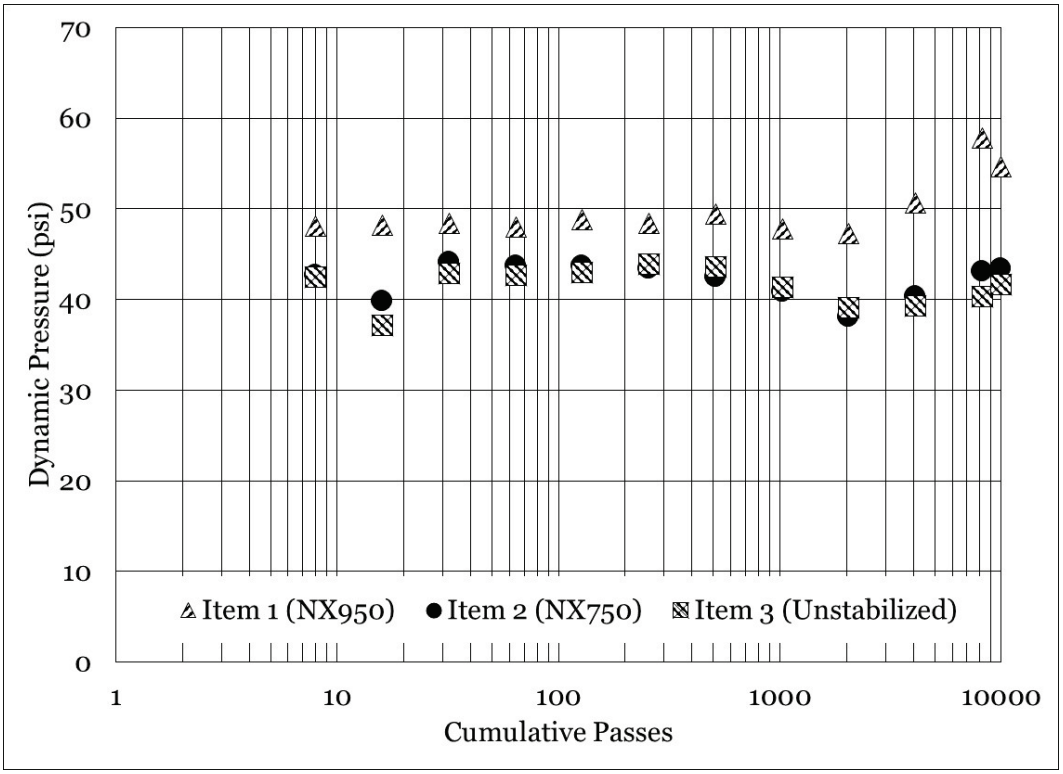

A statistical analysis for mid-depth pressure response is summarized in Table 10. Item 1 (NX950) was found to be statistically different from the other two test items, and Item 1 (NX950) had a higher average MD base pressure in both cases. Statistical comparison of MD base pressure between Item 2 (NX750) and Item 3 (unstabilized) was not found to be statistically significant (p-value = 0.098).

Table 10. Statistical analysis – base pressure response, mid-depth.

Interaction	n	p-value	Significant	Better Performer
Item 1 vs. Item 2	12	<0.001	Yes	Item 1
Item 1 vs. Item 3	12	<0.001	Yes	Item 1
Item 2 vs. Item 3	12	0.098	No	Same

Aggregate base pressure near the bottom of the aggregate layer is presented in Figure 29. A slight increase in measured pressure was observed in all test items early in traffic, i.e., up to approximately 100 passes, which agreed with other EPC measurements. Thereafter, Item 2 (NX750) and Item 3 (unstabilized) remained somewhat consistent for a majority of the test. Item 1 (NX950) trended downward after reaching an early peak, suggesting that the geogrid was effective in reducing pressure with increasing traffic. On average, measured pressure in Item 3 (unstabilized) was 5.2% higher than Item 1 (NX950) and 10.7% higher than Item 2 (NX750). Thus, both geogrids appeared to be effective in reducing measured pressure near the bottom of the aggregate layer.

Figure 29. Maximum measured aggregate pressure (bottom) with traffic.

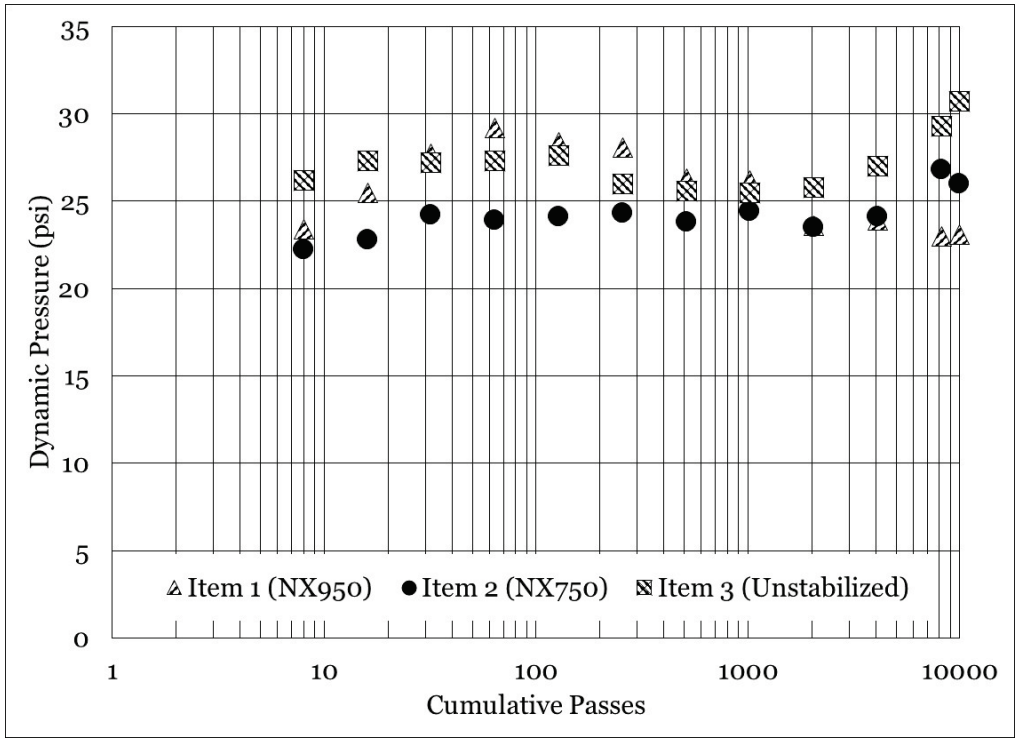

A statistical analysis (Table 11) found that differences in Item 1 (NX950) and the other test items were not statistically significant. The comparison

between Item 2 (NX750) and Item 3 (unstabilized) was found to be significant, and Item 2 (NX750) had a lower average measured pressure near the bottom of the aggregate layer.

Table 11. Statistical analysis – base pressure response, bottom.

Interaction	n	p-value	Significant	Better Performer
Item 1 vs. Item 2	12	0.086	No	Same
Item 1 vs. Item 3	12	0.144	No	Same
Item 2 vs. Item 3	12	<0.001	Yes	Item 2

7.5 Single-depth deflectometer

Single-depth deflectometer response measurements were analyzed to determine dynamic and accumulated deflections. Dynamic deflection measurements considered only the response from the test tire moving over each sensor and included the local minimum and maximum value for each event. Accumulated deflections considered the shift in initial baseline from the beginning of traffic, i.e., pass zero, to the baseline at the end of each data collection point. Thus, accumulated deflection values represent permanent deformation near the top of the subgrade.

Measured dynamic deflections are presented in Figure 30. Dynamic deflection tended to be equivalent for all three test items up to approximately 100 passes, after which performance differences began to emerge. Item 3 (unstabilized) was observed to have the highest dynamic subgrade deflection, which was expected due to the lack of geogrid inclusion. Item 2 (NX750) had slightly lower dynamic deflection than Item 3 (unstabilized). Item 1 (NX950) had the least measured dynamic subgrade deflection, which could be attributed to the larger rib width and rib height of NX950. Dynamic subgrade deflection in Item 1 (NX950) was an average of 20.0% less than Item 3 (unstabilized) and 9.5% less than Item 2 (NX750). Item 2 (NX750) dynamic deflections were approximately 9.6% less than Item 3 (unstabilized). Percentage reductions were similar to observed reductions in measured subgrade pressure, reinforcing the proposition that the geogrids were successful in protecting the subgrade.

Figure 30. Dynamic SDD response with traffic.

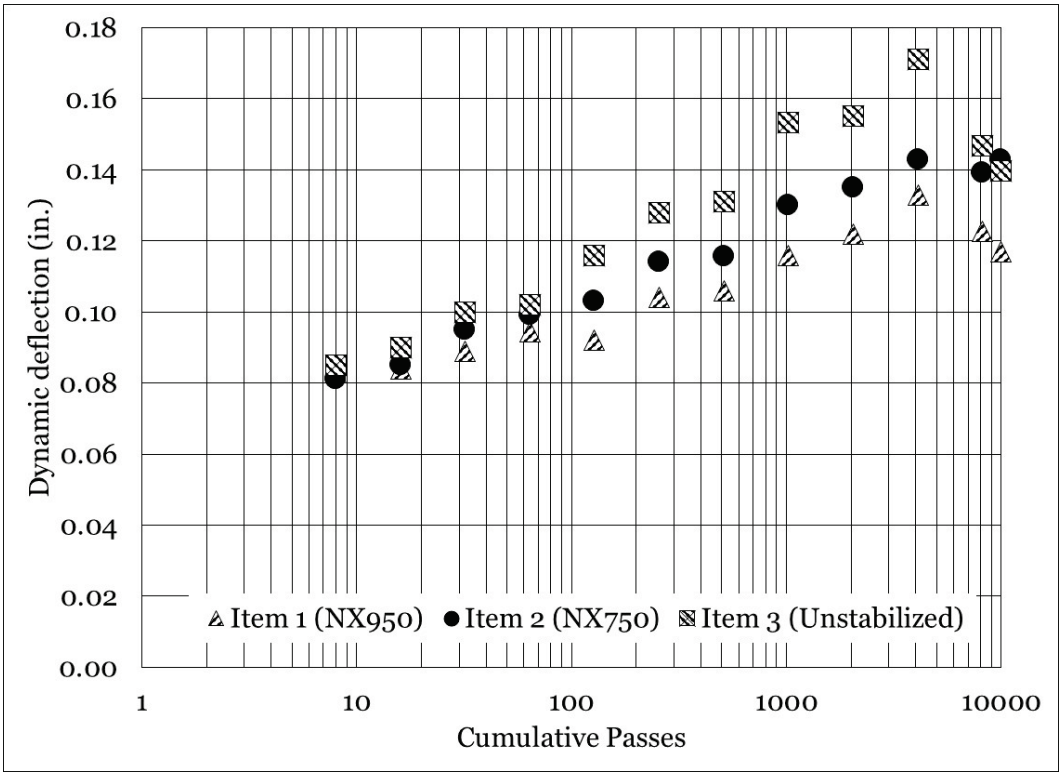

Measured accumulated deflections for each test item (Figure 31) showed similar trends. Item 3 (unstabilized) had the highest accumulated subgrade deflection, followed by Item 2 (NX750) and Item 1 (NX950). Accumulated deflection in Item 1 (NX950) was approximately 17.9% less than Item 3 (unstabilized) and approximately 4.5% less than Item 2 (NX750). Item 2 (NX750) accumulated deflection was approximately 12.9% less than Item 3 (unstabilized). Thus, comparable to dynamic deflection, it could be suggested that the geogrids were effective in reducing long-term permanent deflection, i.e., damage, of the subgrade layer.

A relatively sharp decrease in dynamic SDD response was observed in Item 1 (NX950) and Item 3 (unstabilized) after approximately 4,000 passes and was unexpected. A further review of the Item 1 (NX950) response signal did not suggest that a gauge malfunction occurred, i.e., a clear response with little electronic noise was observed. Additionally, a review of accumulated deflection values did not reveal a similar decrease, further suggesting the gauge was indeed functioning properly. Comparatively, a meaningful increase in measured mid-depth aggregate pressure response was observed during the same data collection intervals. Coupling these observations could suggest that an aggregate

stiffness enhancement via improved aggregate interlock occurred thereby reducing the dynamic SDD response.

Similarly, an in-depth review of the Item 3 (unstabilized) response signal was performed; it was found that the SDD appeared to be functioning properly. Conversely to Item 1 (NX950) observations, accumulated deflection values in Item 3 (unstabilized) experienced a similar decrease to dynamic values. A review of data collected from other sensors, i.e., pressure response values, did not reveal a meaningful change that could enlighten the SDD observations. It is hypothesized that slippage occurred between the LVDT and the LVDT attachment flange. This could explain changes in both dynamic and accumulated deflections, while the sensor was still functioning properly, electronically speaking. Thus, the final SDD observations for Item 3 should be interpreted with caution.

A statistical analysis of SDD response is presented in Table 12 and includes both dynamic and accumulated deflection comparisons. In terms of dynamic deflection, all comparisons were found to be statistically significant. Item 1 (NX950) had lower average dynamic deflection than Item 2 (NX750) and Item 3 (unstabilized), which was expected given that NX950 had larger rib width and rib height. Item 2 (NX750) had lower average dynamic deflections than Item 3 (unstabilized). In terms of accumulated deflection, the statistical analysis indicated that differences in the two geogrids were unremarkable. However, differences between the individual geogrid test items and the unstabilized test item were found to be statistically significant, suggesting that the geogrids were effective in reducing permanent deformation at the top of the subgrade.

Figure 31. Accumulated SDD response with traffic.

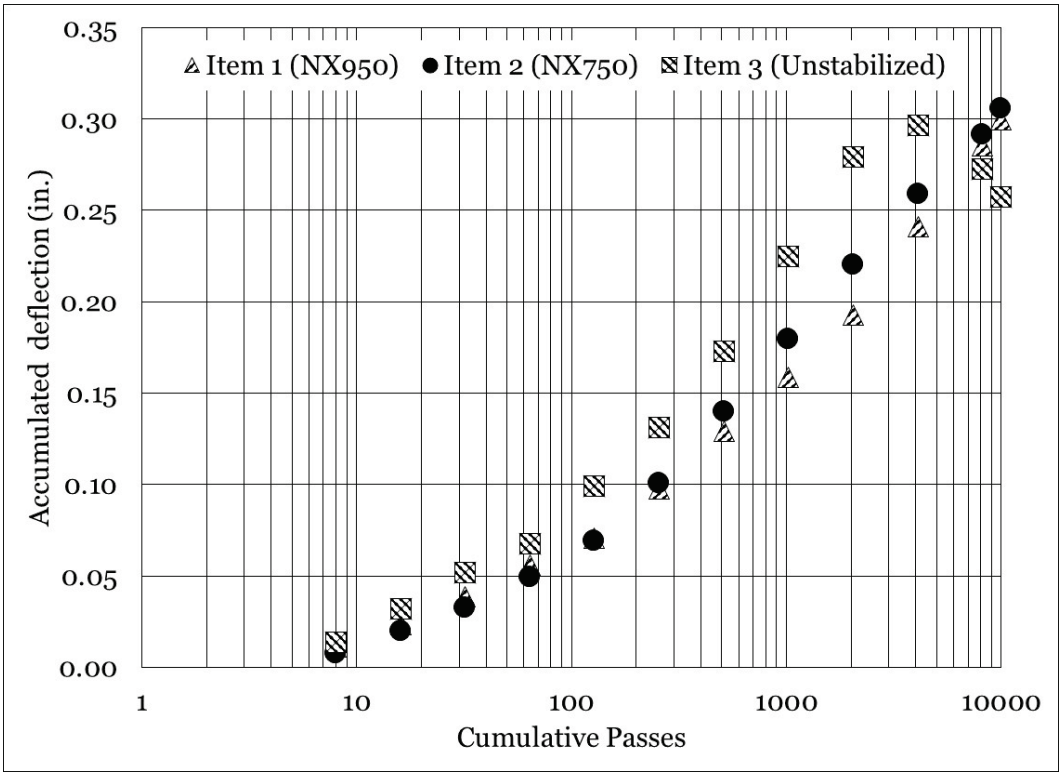

Table 12. Statistical analysis – SDD response.

Dynamic deflection				
Interaction	n	p-value	Significant	Better Performer
Item 1 vs. Item 2	12	0.001	Yes	Item 1
Item 1 vs. Item 3	12	<0.001	Yes	Item 1
Item 2 vs. Item 3	12	0.002	Yes	Item 2
Accumulated deflection				
Interaction	n	p-value	Significant	Better Performer
Item 1 vs. Item 2	12	0.099	No	Same
Item 1 vs. Item 3	12	0.035	Yes	Item 1
Item 2 vs. Item 3	12	0.047	Yes	Item 2

7.6 Bender element response

A literature review suggested that there are varying methodologies for the interpretation of bender element response data, particularly the designation of arrival time (Viggiani and Atkinson 1995; Arulnathan et al. 1998; Fonseca et al. 2008; Gu et al. 2015; Kang et al. 2021). Some have suggested that arrival time is the first indication of the received signal, while others have suggested an input peak to received peak

methodology. An example of the different arrival time selection methods is shown in Figure 32. For the data obtained from this study, both methodologies were used to select signal arrival times such that meaningful comparisons could be made.

A summary of the arrival times and subsequent calculated values are presented in Table 13. In all cases, it was observed that arrival time tended to increase with an increase in traffic, resulting in a decrease in calculated modulus values. Bender element readings prior to traffic application suggested that the calculated modulus values were higher 4 in. above the geogrid when compared to modulus values directly above the geogrid. This could be attributed to a density gradient in the aggregate layer that resulted from placing and compacting the 10-in.-thick layer in one lift, i.e., density was higher closer to the surface.

A series of equality plots were generated to observe the relationship between BE0 and BE4 and are shown in Figure 33. The equality plots revealed that the modulus value obtained from BE4 was almost entirely above the line of equality, indicating that the modulus at BE4 was higher than the modulus at BE0. This was an unexpected finding, as it was anticipated that the modulus would be higher closer to the geogrid. However, it is hypothesized that the extremely soft subgrade could have influenced shear-wave transmission, i.e., dampened the signal, and that migration of the clay subgrade during traffic application (observed during the forensic investigation and described in Chapter 7) could have changed local modulus values.

Modulus based on first arrival time with traffic is shown in Figure 34. Calculated modulus trended downward with an increase in traffic, suggesting that damage was occurring in the aggregate layer. A review of the best-fit regression equations indicated that modulus deterioration decreased closer to the geogrid, i.e., slope of -33.93 at BE0 versus -62.13 at BE4. The trend lines tended to indicate that modulus values were nearly equal at the conclusion of traffic.

Modulus based on peak-to-peak time with traffic is shown in Figure 35. Similar to first arrival time modulus values, a downward trend was observed with increasing traffic. Contrary to first arrival time values, the best fit regression equations indicated that modulus near the geogrid deteriorated more rapidly than modulus values further from the

geogrid. Additionally, modulus values at the different depths tended to diverge with increasing traffic.

A statistical analysis of first arrival time modulus values found that observed differences in BE0 and BE4 were statistically significant (p-value = 0.003, n = 13). Average modulus values were found to be higher at BE4 than modulus values at BE0. Similarly, peak-to-peak modulus values were found to be statistically significant (p-value <0.001, n =13), and BE4 was found to be higher than BE0.

Figure 32. Example of bender element signal response.

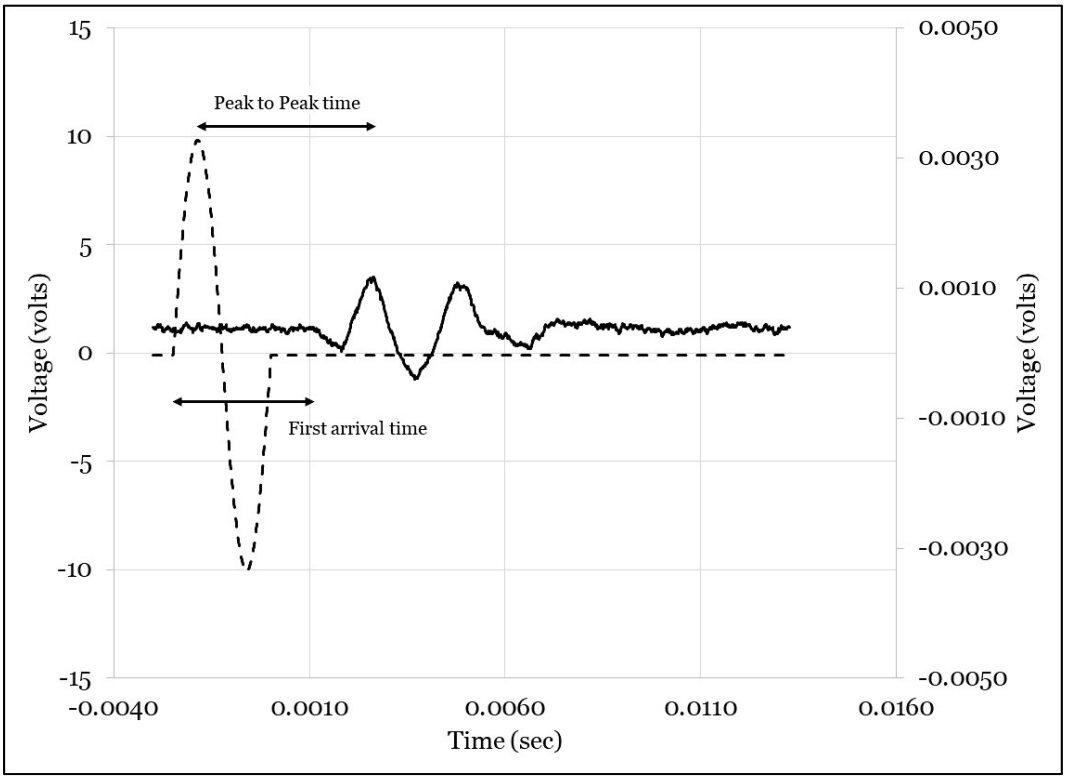

Table 13. Bender element response summary.

Frequency (hz)	400				Density (kN/m^3)		22.46	
L tip-tip (m)	1.151				Poisson ratio		0.35	
Response based on first arrival time								
	Bender Element 0 (BE0)					Bender Element 4 (BE4)		
Traffic Interval	Time (sec)	V (m/s)	G (Mpa)	E (Mpa)	Time (sec)	V (m/s)	G (Mpa)	E (Mpa)
0	0.003427	335.9	253.4	684.2	0.002872	400.7	360.7	974.0
8	0.003710	310.2	216.2	583.8	0.002960	388.8	339.7	917.1
16	0.003913	294.1	194.3	524.7	0.003020	381.1	326.3	881.0
32	0.004089	281.5	178.0	480.6	0.004141	278.0	173.6	468.6
64	0.003647	315.6	223.7	604.1	0.003512	327.7	241.3	651.5
128	0.004140	278.0	173.6	468.8	0.003499	328.9	243.0	656.2
256	0.004250	270.8	164.8	444.9	0.003059	376.2	318.0	858.5
512	0.005588	206.0	95.3	257.3	0.003847	299.2	201.1	543.1
1024	0.004589	250.8	141.3	381.6	0.004089	281.5	178.0	480.6
2048	0.003725	309.0	214.5	579.2	0.003748	307.1	211.8	572.0
4096	0.004402	261.5	153.6	414.7	0.004622	249.0	139.3	376.1
8192	0.005902	195.0	85.4	230.7	0.004503	255.6	146.8	396.4
10000	0.004751	242.3	131.8	356.0	0.004814	239.1	128.4	346.7
Response based on peak to peak								
0	0.004051	284.1	181.4	489.7	0.004034	285.3	182.9	493.7
8	0.004472	257.4	148.8	401.9	0.004428	259.9	151.8	409.8
16	0.004739	242.9	132.5	357.7	0.004149	277.4	172.9	466.8
32	0.005105	225.5	114.2	308.3	0.005117	225.0	113.7	306.9
64	0.004340	265.2	158.0	426.5	0.004297	267.9	161.2	435.3
128	0.005671	203.0	92.5	249.9	0.004625	248.9	139.2	375.7
256	0.005139	224.0	112.7	304.3	0.004067	283.0	179.9	485.8
512	0.005953	193.3	84.0	226.7	0.005067	227.1	115.9	312.9
1024	0.005538	207.8	97.0	262.0	0.004854	237.1	126.3	341.0
2048	0.005172	222.6	111.3	300.4	0.004493	256.2	147.4	398.0
4096	0.005804	198.3	88.4	238.6	0.004641	248.0	138.2	373.1
8192	0.005904	195.0	85.4	230.6	0.004854	237.1	126.3	341.0
10000	0.005405	213.0	101.9	275.1	0.004739	242.9	132.5	357.7

Figure 33. Equality plots for modulus values from bender element response data.

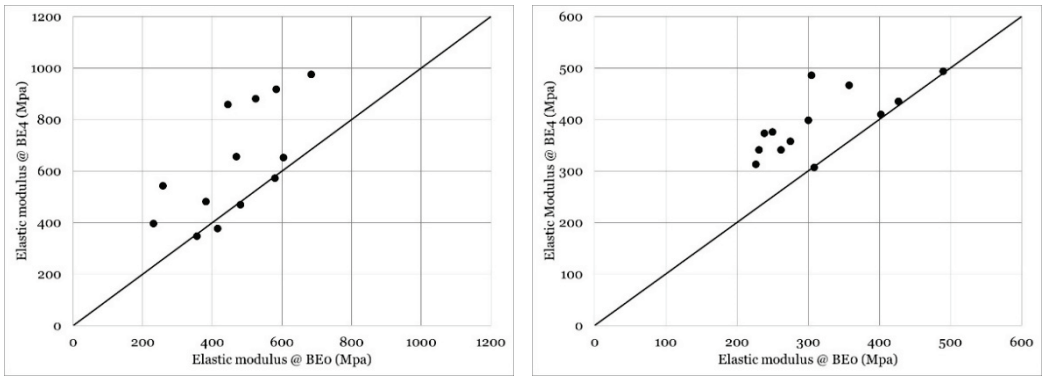

(a) First arrival time (b) Peak to peak

Figure 34. Elastic modulus based on first arrival with traffic.

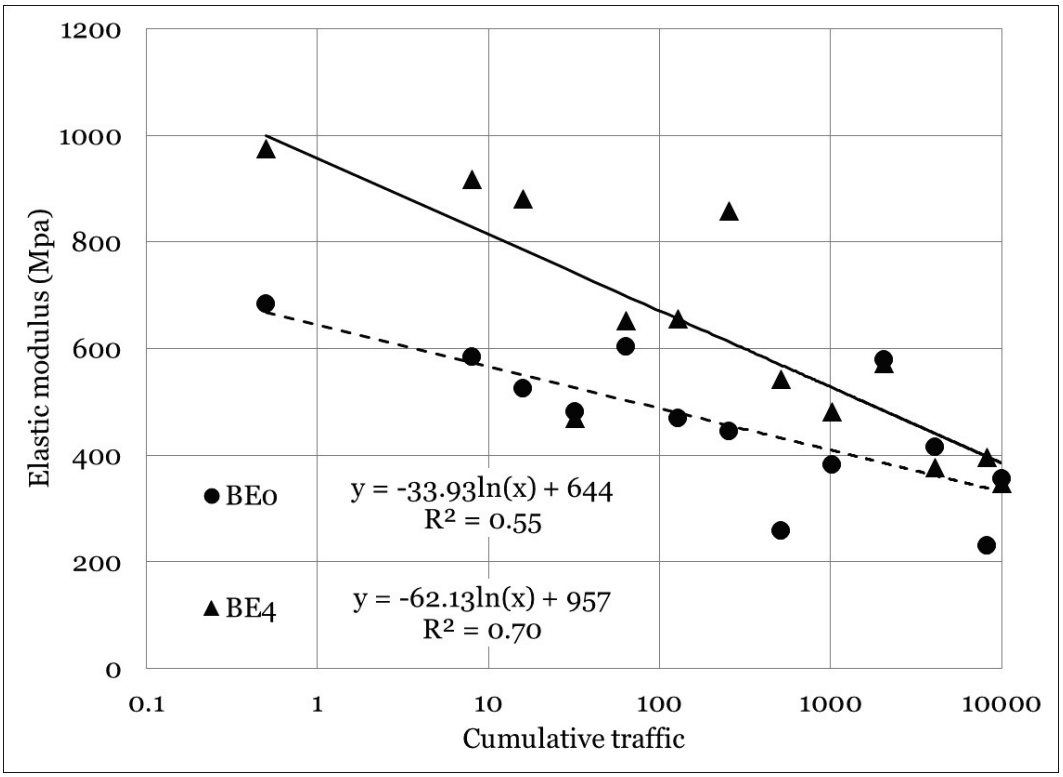

Figure 35. Elastic modulus based on peak to peak with traffic.

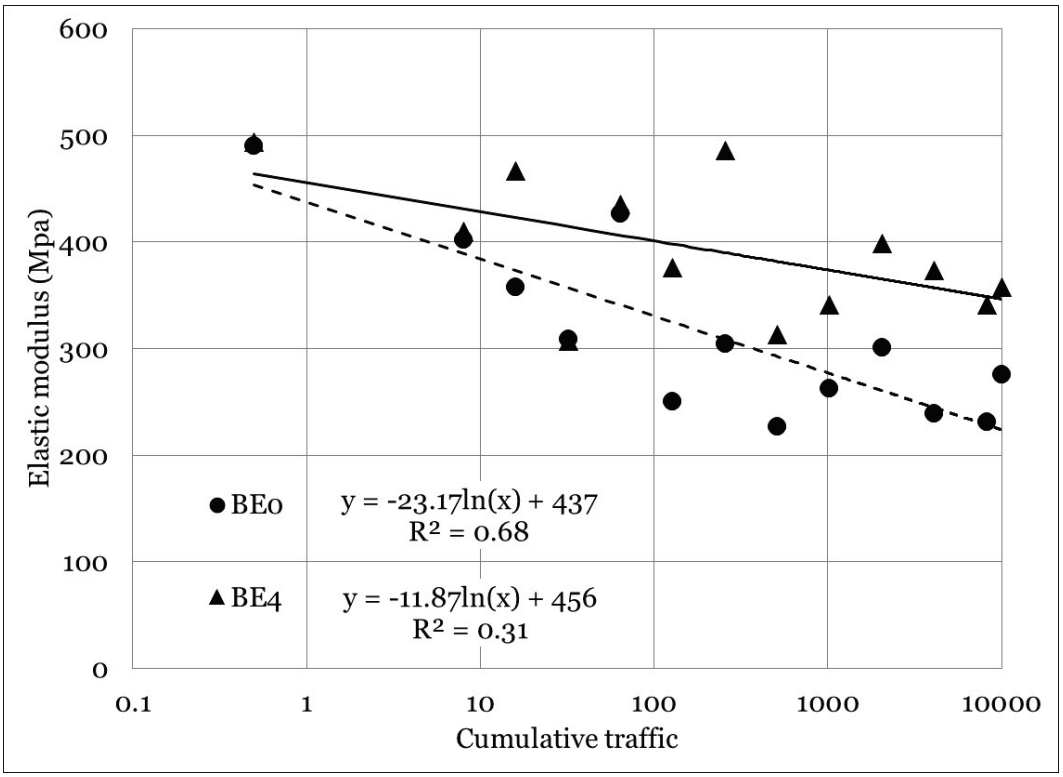

7.7 Uniaxial strain gauge response

Maximum uniaxial strain gauge response values for Item 1 (NX950) are presented in Figure 36. A meaningful amount of variability was observed in initial strain gauge response values, ranging from approximately 500 microstrain on one of the center strain gauges (Center Bottom 5B) up to approximately 1400 microstrain (Center Top 2A). The observed variability could be attributed to gauge adhesion, gauge type, and aggregate interaction at the location of a gauge among other potential construction variabilities. Limited clear trends were observed; however, on average, the data indicated that higher strain values were recorded at the offset gauge locations when compared to the center locations. This suggests that restraint, i.e., tension, was developing near the edges of the wheel path. In general, relatively consistent values were observed up to 1,000 passes, after which an upward trend was noted. Rut depth measurements indicated that the rate of rut development in Item 1 (NX950) appeared to slow after approximately 1,000 passes, thus the observed increase in measured strain may be attributed to a point at which the geogrid fully "engaged" in the pavement section.

Figure 36. Uniaxial strain gauge response for Item 1 (NX950).

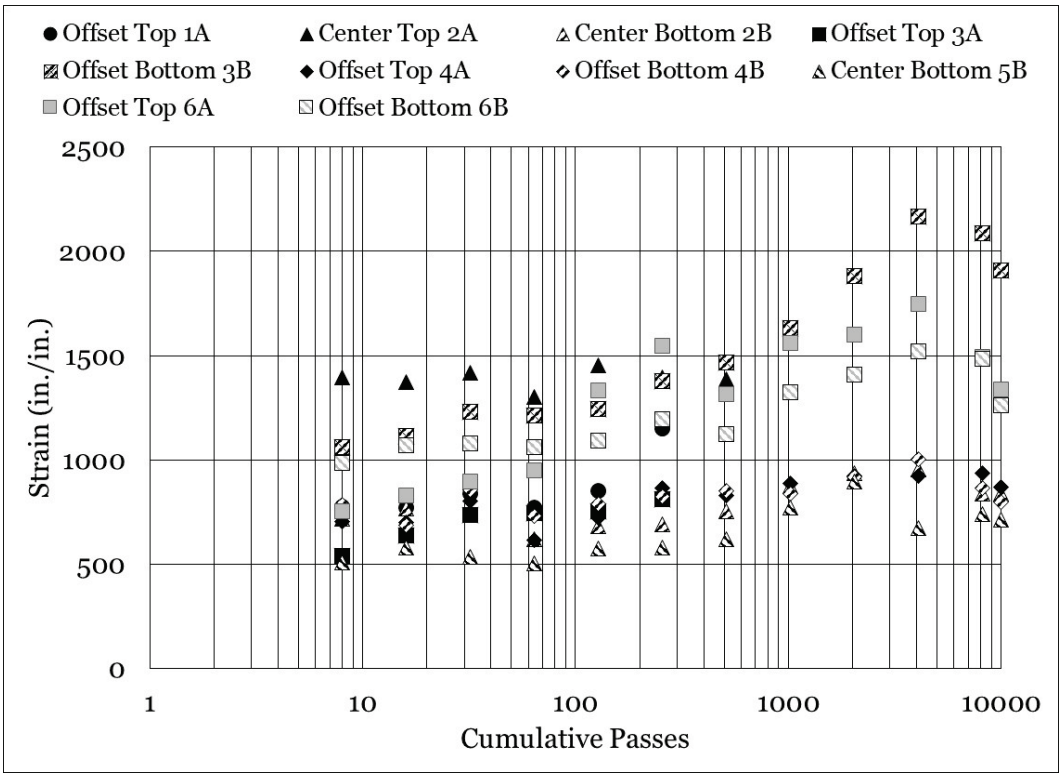

Maximum uniaxial strain gauge response values for Item 2 (NX750) are presented in Figure 37. Similar to strain response values in Item 1 (NX950), a meaningful amount of variability was observed in the Item 2 (NX750) strain gauge response values. Initial strain response values ranged from a low of approximately 400 microstrain in one of the center gauges (Center Bottom 11B) up to approximately 900 microstrain (Offset Bottom 10B). Response values remained somewhat constant during the first 100 passes and trended upward thereafter. A review of rutting data indicated that Item 2 (NX750) rutting rate increased after approximately 100 passes, which could explain the increase in measured strain response.

Strain response in Item 2 (NX750) was observed to be slightly less than strain response in Item 1 (NX950), which was an unexpected result. Simply, more deformation in Item 2 (NX750) would suggest that higher strain values should be observed. Further, it was anticipated that since NX750 had lower rib width and rib height than NX950, higher strain values would be observed. A review of posttest forensic survey data (discussed in detail in Chapter 8) indicated that a wider width of deformation was observed at the top of the subgrade in Item 2 (NX750) when compared to Item 1 (NX950). Essentially, there was a wider rut

"bowl" in the subgrade of Item 2 (NX750) when compared to Item 1 (NX950). Thus, it is hypothesized that the observed wider deformation bowl resulted in a reduction in "bending" of the geogrid in Item 2 (NX750), reducing observed strain values. Simply, the gauges were uniformly pushed downward in Item 2 (NX750), whereas, the confined rut bowl in Item 1 (NX950) induced higher measured strain values.

A review of average response values was made to investigate the difference in the two gauge types utilized in this study. Recall that UXEP had a high-elongation polymide backing with a range of 10% of gauge length, and UXCEA was a grid-encapsulated gauge that had a range of 3% of the gauge length. In terms of survivability, two UXEP gauges were not functional at the beginning of traffic, i.e., did not survive construction, and one UXCEA gauge was not functional at the beginning of traffic. During traffic application, five UXEP gauges failed, and gauge failures began to occur near 500 traffic passes. None of the UXCEA gauges failed during traffic application. Thus, while gauge selection must be tailored to individual geogrid configurations, these observations suggest that, in terms of initial and long-term survivability, the UXCEA gauges would be a preferred selection.

Figure 37. Uniaxial strain gauge response for Item 2 (NX750).

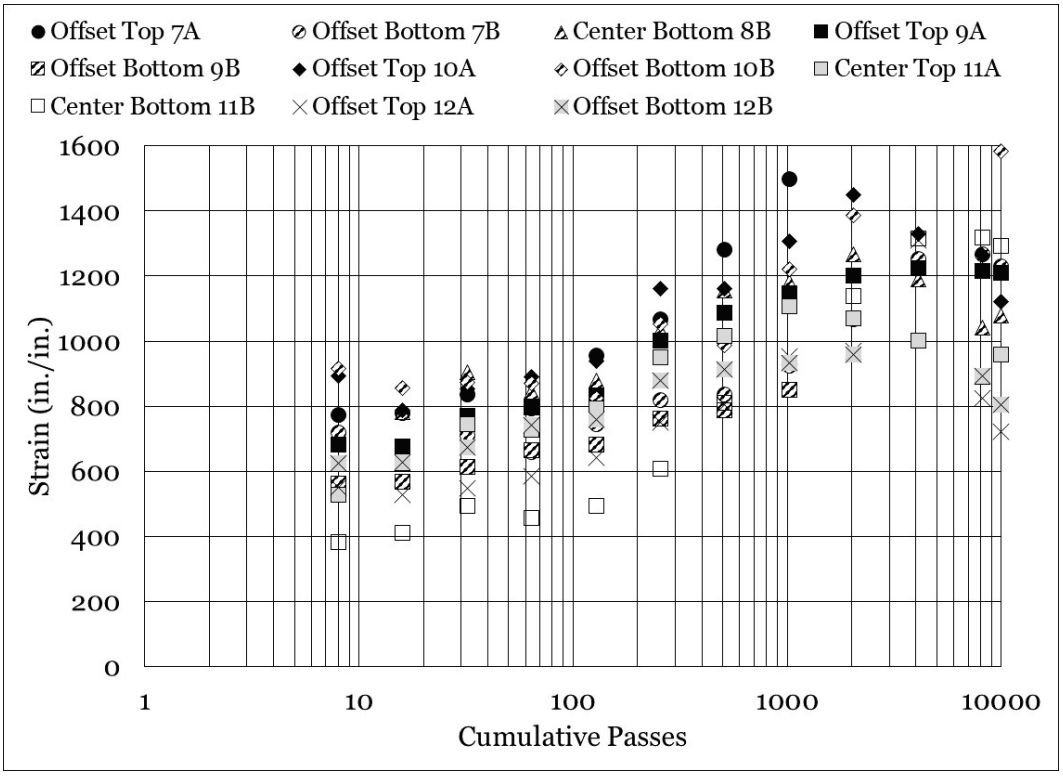

8 Forensic Investigation

At the conclusion of traffic testing, each test item was trenched to investigate pavement failure and to characterize material properties. Trenches were located at the midpoint, i.e., 15 ft from the ends of each test item. Each trench was approximately 3 ft wide and extended across the full traffic lane. In-place CBR tests and nuclear density measurements were made both within the wheel path and outside the wheel path. Additionally, elevation measurements were made at the surface of the subgrade layer. Results of characterization tests performed in the trench locations for each test item are shown in Table 14.

A review of the inside rut (IR) subgrade measurements indicated that an increase in measured compaction was observed in all test items, as expected. Subgrade compaction in Item 1 (NX950) increased by 3.6%, Item 2 (NX750) increased by 2.9%, and Item 3 (unstabilized) increased by 3.7%. Nuclear moisture density measurements indicated that moisture content decreased by approximately 3-4% in the test items. The results of IR CBR tests indicated that essentially no change was observed in measured CBR for all the test items. Oven-dried moisture contents yielded an approximate 1-2% decrease in moisture content across the test section. Thus, the IR measurements suggest that crucial subgrade properties remained relatively consistent throughout the duration of traffic application. Similar observations can be made for material characterization testing conducted outside rut (OR).

A review of IR aggregate surface measurements indicated that a minor increase in compaction was observed in the aggregate surface layer. Aggregate layer compaction increased 0.7% in Item 1 (NX950), 2.3% in Item 2 (NX750), and 0.6% in Item 3 (unstabilized). Most notably, measured IR CBR values were well above 100 in all cases and exceeded the measurement capabilities of the load ring, i.e., the load ring reached maximum load prior to completing each test. These measurements represented a 50 CBR increase from as-built properties. However, if one considers that the aggregate surface was exposed over an approximate two-month period during trafficking, and that, over that time, measured moisture content decreased from approximately 3% to 1%, it is postulated that natural cementation of the limestone aggregate increased measured CBR.

Table 14. Summary of posttest properties.

Property	Item 1 (NX950)	Item 2 (NX750)	Item 3 (Unstabilized)
CH Subgrade (MDD =106.1 pcf @ OMC = 17.1%)[1]			
IR Wet Density (pcf)	114.4	114.1	114.8
IR Dry Density (pcf)	87.3	85.7	86.3
IR Nuclear Moisture Content (%)	31.1	33.2	33.1
IR Compaction (%)	82.3	80.8	81.3
IR Oven-Dried Moisture (%)	39.2 ± 0.3	38.2 ± 0.2	39.7 ± 1.1
IR In-Place CBR (%)	2.1 ± 0.2	2.2 ± 0.2	2.0 ± 0.2
OR Wet Density (pcf)	113.9	114.2	113.0
OR Dry Density (pcf)	85.3	85.7	86.1
OR Nuclear Moisture Content (%)	33.5	33.3	31.3
OR Compaction (%)	80.4	80.8	81.1
OR Oven-Dried Moisture (%)	37.5 ± 0.5	38.5 ± 0.6	39.1 ± 1.1
OR In-Place CBR (%)	2.9 ± 0.2	2.5 ± 0.1	2.1 ± 0.1
Aggregate Surface (MDD = 147.9 pcf @ OMC = 5.2%)[1]			
IR Wet Density (pcf)	144.9	144.1	140.6
IR Dry Density (pcf)	142.6	141.7	138.5
IR Nuclear Moisture Content (%)	1.6	1.7	1.5
IR Compaction (%)	96.4	95.8	93.6
IR Oven-Dried Moisture (%)	1.0 ± 0.2	1.0 ± 0.2	1.1 ± 0.3
IR In-Place CBR (%)	100+	100+	100+
OR Wet Density (pcf)	140.6	141.9	139.5
OR Dry Density (pcf)	138.1	139.5	137.7
OR Nuclear Moisture Content (%)	1.8	1.7	1.3
OR Compaction (%)	93.4	94.3	93.1
OR Oven-Dried Moisture (%)	0.7 ± 0.1	0.5 ± 0.1	0.7 ± 0.1
OR In-Place CBR (%)	100+	100+	100+

[1]Maximum dry density and optimum moisture content as determined from ASTM D1557; MDD = maximum dry density; OMC = optimum moisture content; CBR = California bearing ratio; IR = inside rut; OR = outside rut

The aggregate layer was carefully excavated to expose the underlying geogrids for visual inspection (Figure 38 and Figure 39). Visual inspection indicated that the geogrids were intact and that no damage was sustained during construction or trafficking. Indentations were observed in the subgrade of Item 1 (NX950) and Item 2 (NX750), indicating aggregate

strike-through and interlock with the geogrids. It was noted that the soft subgrade migrated into the aggregate layer directly above the geogrids (Figure 40). Photographs showing the excavated cross sections for each test item are shown in Figure 41 through Figure 43.

Figure 38. Item 1 (NX950) excavated geogrid.

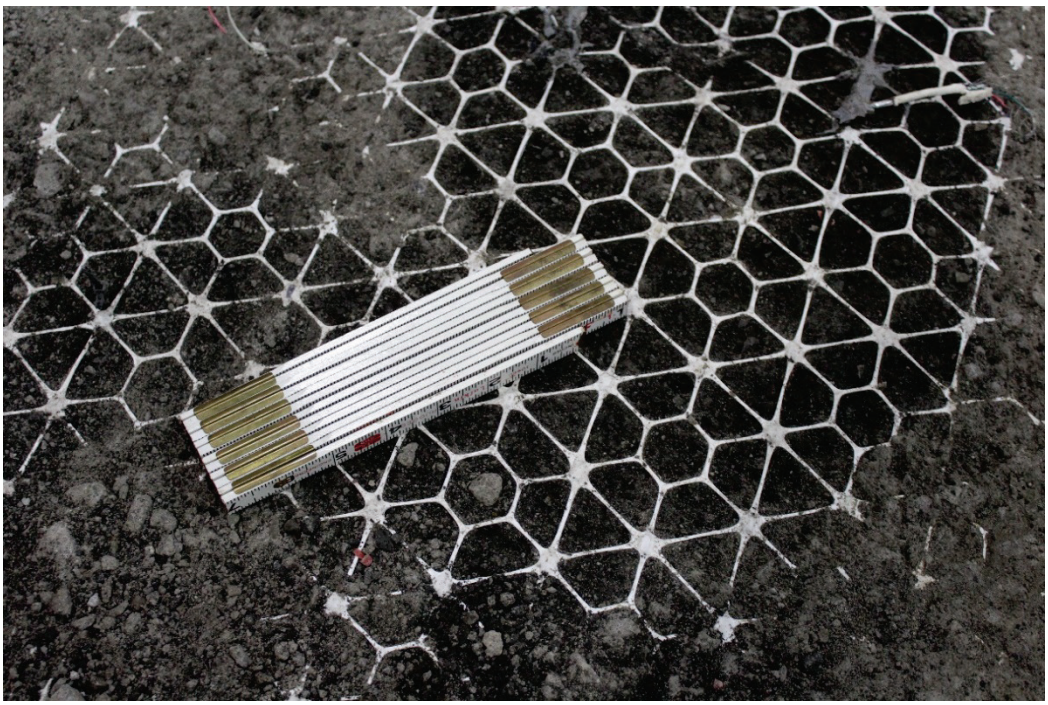

Figure 39. Item 2 (NX750) excavated geogrid.

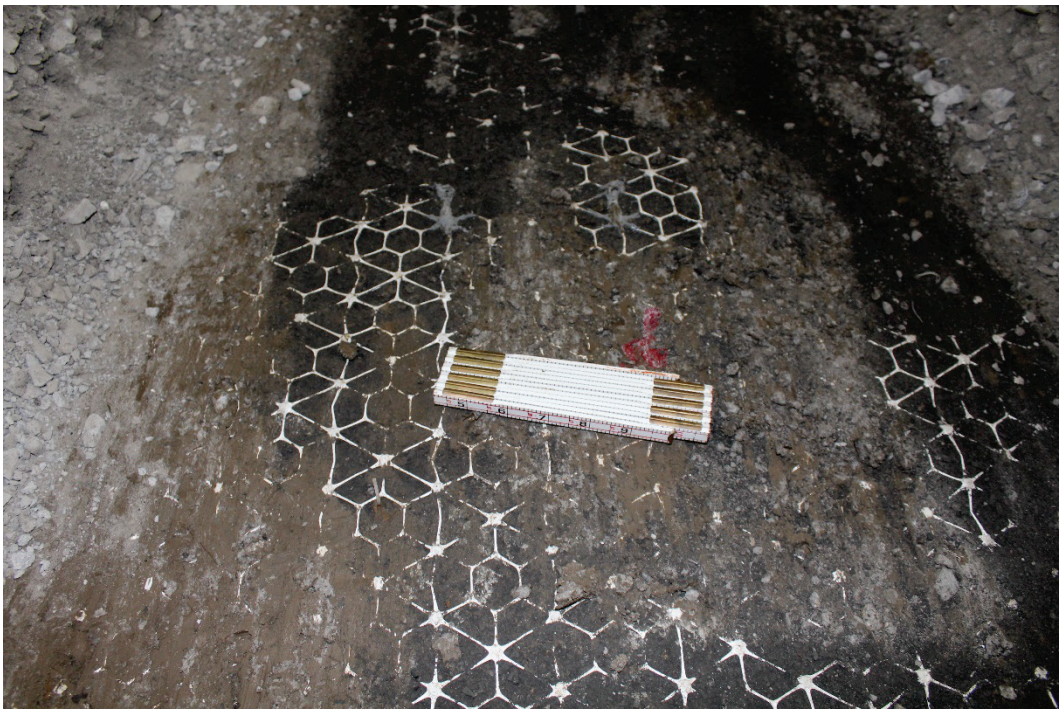

Figure 40. Migration of clay subgrade above geogrid.

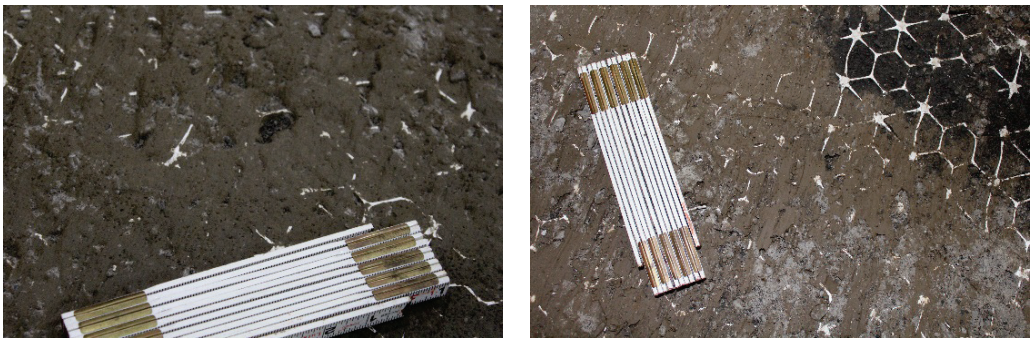

(a) Item 1 (NX950) clay migration (b) Item 2 (NX750) clay migration

Posttest elevation measurements were made at the surface of the aggregate layer and subgrade. The measurements indicated that little rutting occurred in the Item 1 (NX950) subgrade, i.e., approximately 0.25 in., which was confirmed by visual inspection (Figure 44). Approximately 0.4 in. of rutting was measured in the subgrade of Item 2 (NX750) (Figure 45), and approximately 1.4 in. of rutting was observed in the subgrade of Item 3 (unstabilized) (Figure 46). Further, upheaval was observed in the subgrade layer outside the wheel path of Item 3 (unstabilized) but was not observed in Item 1 (NX950) or Item 2 (NX750). Thus, the posttest survey data confirms that the geogrids were successful in improving deformation performance in all layers of the pavement structure.

Figure 41. Item 1 (NX950) posttest excavation.

Figure 42. Item 2 (NX750) posttest excavation.

Figure 43. Item 3 (unstabilized) posttest excavation.

Figure 44. Item 1 (NX950) posttest layer elevation.

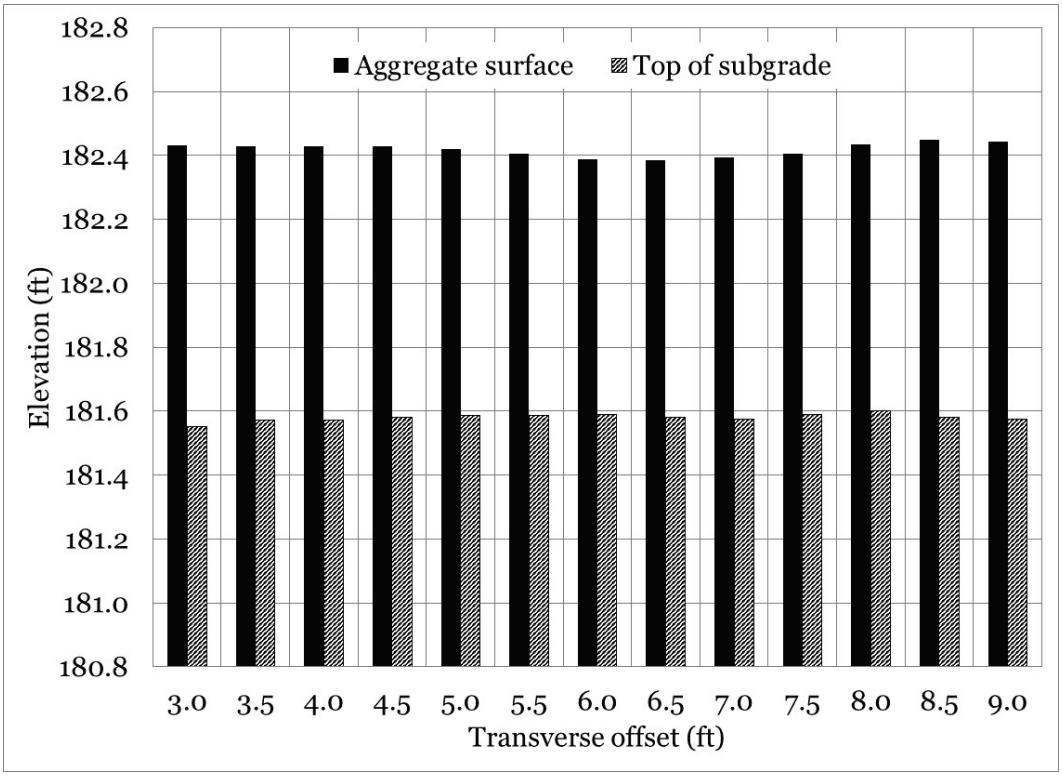

Figure 45. Item 2 (NX750) post-test elevation.

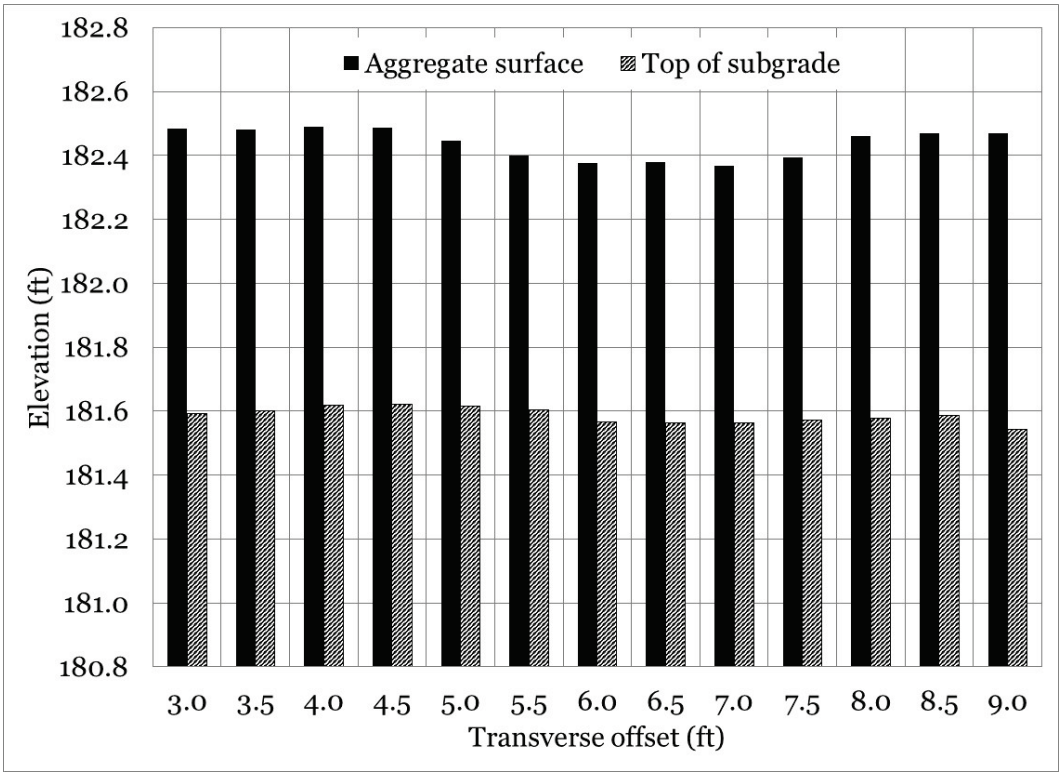

Figure 46. Item 3 (unstabilized) post-test elevation.

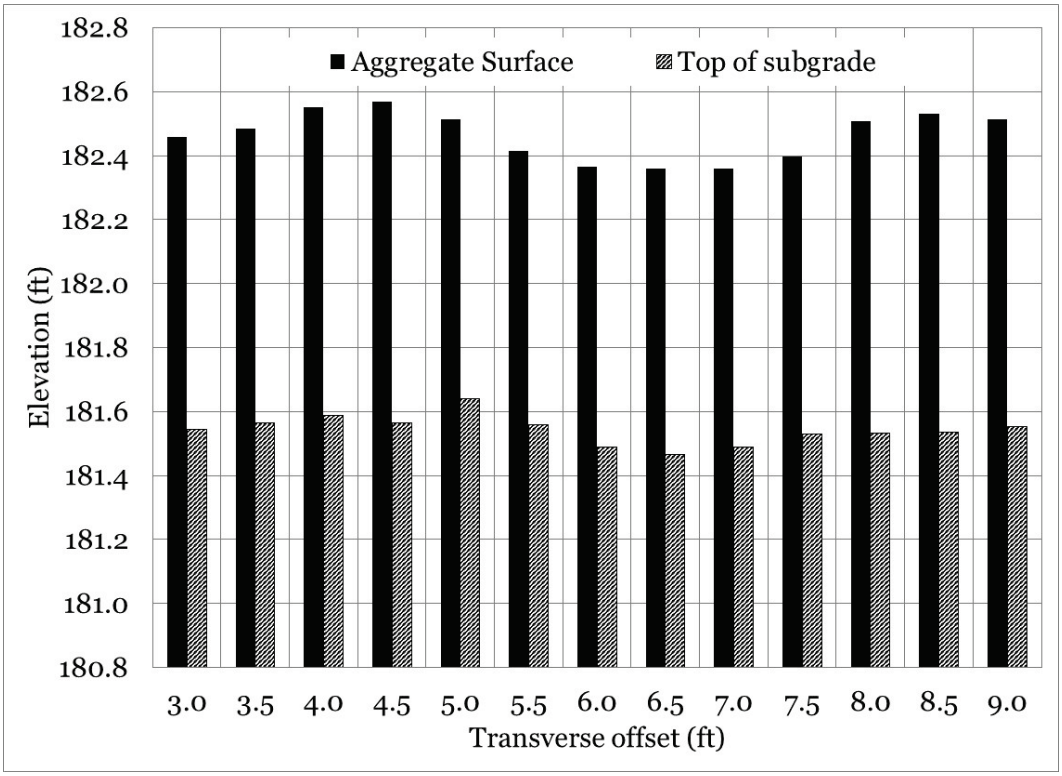

9 Conclusions

A full-scale test section was constructed to evaluate the performance of prototype geogrids in an unsurfaced pavement structure. The construction and traffic data were analyzed to assess the performance of the prototype geogrids relative to each other, as well as, relative to an unstabilized control section. The test items were constructed and trafficked simultaneously allowing for meaningful performance to be made. Analysis of the test results yielded the following conclusions.

1. As-built properties suggested that the multi-axial geogrids improved compaction and reduced compaction variability in the aggregate layer.
2. The inclusion of the multi-axial geogrids resulted in significant rutting improvements when compared to the unstabilized control test item. Further, upheaval outside the wheel path was less in the geogrid test items than the unstabilized control.
3. Item 1, which contained NX950, was found to be the best rutting performer and had approximately 0.6 in. of rutting at the conclusion of traffic. Item 2, which contained NX750, was the next best performer and had 1.0 in. of rutting. Comparatively, Item 3, the unstabilized control, had 2.4 in. of rutting at the conclusion of traffic.
4. Impulse stiffness modulus, determined from falling weight deflectometer measurements, suggested some initial stiffening was provided from geogrid inclusion. Item 1 (NX950) was found to be statistically different (higher) than Item 2 (NX750) and Item 3 (unstabilized), and ISM differences in Item 2 (NX750) and Item 3 (unstabilized) were unremarkable.
5. Subgrade pressure response measurements indicated that geogrid inclusion provided minor pressure reductions early in traffic, but a more meaningful reduction, i.e., on the order of 14 to 16%, were observed near the final data collection points. Thus, it can be concluded that the geogrids were effective in reducing measured pressure on the subgrade.
6. Single-depth deflectometer measurements indicated that geogrid inclusion reduced dynamic deflection on the subgrade from 10 to 20%. Similar reductions were observed in accumulated, i.e., permanent, deflection. Thus, it can be concluded that the geogrids were effective in reducing measured deflection on the subgrade.
7. Measured mid-depth aggregate pressure was found to be approximately 16% higher in the geogrid test items when compared to the unstabilized control item. This suggests that geogrid inclusion stiffened the aggregate

layer and resulted in a redistribution of applied pressure higher in the pavement structure.

8. Pressure measured at the bottom of the aggregate layer was found to be 5 to 10% lower in the geogrid test items when compared to the unstabilized control. These data agree with pressure measurements in the subgrade and support the hypothesis of a redistribution of applied pressure.
9. Bender element data suggested that the aggregate layer was stiffer 4 in. above the geogrid when compared to directly above the geogrid. The relationship between modulus values and traffic varied based on the methodology used to select signal arrival time, thus these data should be interpreted with caution.
10. Increases in measured geogrid strain values tended to coincide with changes in the rate of rutting development, suggesting that the geogrids were being mobilized in the pavement section.
11. A forensic investigation indicated minimal changes were observed in subgrade CBR, indicating that subgrade support conditions were consistent throughout traffic application. Increased CBR was measured in the aggregate layer and could be attributed to natural cementation as a result of exposure.

The following recommendations are a result of this study.

1. It is recommended that the geogrids evaluated in this study be evaluated in a surfaced, i.e., paved, cross section to further evaluate performance in a higher traffic scenario to determine if similar rutting enhancements can be gained.
2. It is recommended that laboratory tests, i.e., tensile tests, be conducted of strain-gauge instrumented geogrid specimens to fully understand the relationship between field-measured strain and applied load.
3. Installation and collection of bender element data were found to be successful under controlled traffic conditions. It is recommended that bender elements be included in future full-scale pavement studies to support analysis of the geogrid/aggregate interaction.

References

AASHTO (Association of American Highway and Transportation Officials). 2012. *Standard specification for classification of soils and soil-aggregate mixtures for highway construction purposes*. AASHTO M 145. Washington, DC: AASHTO.

Arulnathan, R., R. W. Boulanger, and M. F. Riemer. 1998. Analysis of bender element tests. *Geotechnical Testing Journal* 21(2): 120-131.

ASTM (American Society for Testing and Materials). 2009. *Standard test method for CBR (California Bearing Ratio) of soils in place*. Designation: D 4429-09a. West Conshohocken, PA: ASTM International.

_____. 2012. *Standard test method for laboratory compaction characteristics of soil using modified effort (56,000 ftblf/ft3 [2,700 kN-m/m3])*. Designation: D 1557-12e1. West Conshohocken, PA: ASTM International.

_____. 2016. *Standard test method for California Bearing Ratio (CBR) of laboratory-compacted soils*. Designation: D 1883-16. West Conshohocken, PA: ASTM International.

_____. 2017a. *Standard practice for classification of soils for engineering purposes (Unified Soil Classification System)*. Designation: D 2487-17. West Conshohocken, PA: ASTM International.

_____. 2017b. *Standard test methods for in-place density and water content of soil and soil-aggregate by nuclear methods (shallow depth)*. Designation: D 6938-17a. West Conshohocken, PA: ASTM International.

_____. 2017c. *Standard test methods for liquid limit, plastic limit, and plasticity index of soils*. Designation: D4318-17c1. West Conshohocken, PA: ASTM International.

_____. 2018. *Standard test method for use of the dynamic cone penetrometer in shallow pavement applications*. Designation: D 6951/6951M-18. West Conshohocken, PA: ASTM International.

Fonseca, A. V., C. Ferreira, and M. Fahey. 2008. A framework interpreting bender element tests, combining time-domain and frequency-domain methods. *Geotechnical Testing Journal* 32(2): 91-107.

Gu, X., J. Yang, M. Huang, and G. Gao. 2015. Bender element tests in dry and saturated sand: signal interpretation and result comparison. *Soils and Foundations* 55(5): 951-962.

Huang, Y. H. 2004. *Pavement analysis and design*. Upper Saddle River, NJ: Pearson Education Inc.

Kang, M., I. I. A. Gamhia, E. Tutumluer, W. T. Hong, and J. S. Tingle. 2021. Bender element field sensor for the measurement of pavement base and subbase stiffness characteristics. *Transportation Research Record: Journal of the Transportation Research Board* DOI: 10.1177/0361198121998350.

Norwood, G. J., and J. S. Tingle. 2014. *Performance of geogrid-stabilized gravel flexible base with bituminous surface treatment*. ERDC/GSL-TR-14-15. Vicksburg, MS: U.S. Army Engineer Research and Development Center.

Robinson, W. J., J. S. Tingle, and G. J. Norwood. 2017. *Full-scale accelerated testing of multi-axial geogrid stabilized flexible pavements*. ERDC/GSL-TR-17-9. Vicksburg, MS: U.S. Army Engineer Research and Development Center.

Viggiani, G., and Atkinson, J. H. 1995. Interpretation of bender element tests. *Geotechnique* 45(1): 149-154.

Appendix A: Deformation Data

Test Item	Item 1	Item 2	Item 3
Pass	Average Rut Depth (in.)		
0	0.00	0.00	0.00
8	0.10	-0.04	0.02
16	0.06	0.06	-0.04
32	0.13	-0.06	-0.04
64	0.13	0.02	-0.02
128	0.15	0.10	0.04
256	0.21	0.19	0.21
512	0.27	0.29	0.35
1,024	0.33	0.38	0.63
2,048	0.42	0.63	1.04
4,096	0.46	0.79	1.60
8,192	0.54	0.92	2.31
10,000	0.58	1.04	2.40

Test Item	Item 1	Item 2	Item 3
Pass	Average Permanent Deformation (in.)		
0	0.00	0.00	0.00
8	0.07	0.08	0.10
16	0.04	0.07	0.10
32	0.06	0.08	0.17
64	0.17	0.20	0.26
128	0.19	0.22	0.31
256	0.46	0.50	0.64
512	0.32	0.38	0.58
1,024	0.40	0.60	0.83
2,048	0.39	0.70	1.07
4,096	0.48	0.91	1.50
8,192	0.60	1.11	1.92
10,000	0.64	1.18	2.00

Appendix B: Pressure Cell Response Data

Subgrade vertical pressure			
Test Item	Item 1	Item 2	Item 3
Pass	Dynamic vertical pressure (psi)		
8	18.6	18.8	18.8
16	18.5	18.9	19.3
32	19.1	19.4	20.2
64	20.1	19.7	20.6
128	19.2	20.0	21.6
256	19.9	20.0	20.5
512	19.3	20	20.1
1,024	19.6	20.3	19.6
2,048	18.9	19.4	19.2
4,096	19.0	19.4	21.2
8,192	19.2	20.0	22.7
10,000	19.5	19.6	23.3

Aggregate vertical pressure (mid-depth)			
Test Item	Item 1	Item 2	Item 3
Pass	Dynamic vertical pressure (psi)		
8	48.1	42.7	42.5
16	48.2	39.8	37.1
32	48.4	44.1	42.9
64	48.0	43.7	42.7
128	48.8	43.7	43.0
256	48.4	43.4	43.9
512	49.4	42.5	43.6
1,024	47.8	40.8	41.3
2,048	47.3	38.1	39.1
4,096	50.6	40.3	39.3
8,192	57.8	43.1	40.3
10,000	54.6	43.4	41.6

Aggregate vertical pressure (bottom)			
Test Item	Item 1	Item 2	Item 3
Pass	Dynamic vertical pressure (psi)		
8	23.4	22.2	26.2
16	25.5	22.8	27.3
32	27.7	24.2	27.2
64	29.2	23.9	27.3
128	28.4	24.1	27.6
256	28.1	24.3	26.0
512	26.3	23.8	25.6
1,024	26.2	24.4	25.5
2,048	23.6	23.5	25.8
4,096	23.9	24.1	27.0
8,192	23.0	26.8	29.3
10,000	23.1	26.0	30.7

Appendix C: Single-depth Deflectometer Response Data

Single depth deflectometer response			
Test Item	Item 1	Item 2	Item 3
Pass	Dynamic SDD response (in.)		
8	0.083	0.081	0.085
16	0.084	0.085	0.090
32	0.089	0.095	0.100
64	0.094	0.099	0.102
128	0.092	0.103	0.116
256	0.104	0.114	0.128
512	0.106	0.116	0.131
1,024	0.116	0.130	0.153
2,048	0.122	0.135	0.155
4,096	0.133	0.143	0.171
8,192	0.123	0.139	0.147
10,000	0.117	0.143	0.140

Single depth deflectometer response			
Test Item	Item 1	Item 2	Item 3
Pass	Accumulated SDD response (in.)		
8	0.011	0.007	0.014
16	0.023	0.020	0.032
32	0.039	0.032	0.052
64	0.056	0.049	0.068
128	0.071	0.069	0.099
256	0.097	0.101	0.131
512	0.129	0.140	0.173
1,024	0.159	0.179	0.225
2,048	0.193	0.220	0.279
4,096	0.241	0.259	0.297
8,192	0.285	0.291	0.272
10,000	0.300	0.305	0.257

Appendix D: Uniaxial Strain Gauge Response Data

Uniaxial strain gauge response										
Location	O	C	C	O	O	O	O	C	O	O
Side	T	T	B	T	B	T	B	B	T	B
ID	1A	2A	2B	3A	3B	4A	4B	5B	6A	6B
Gauge Type	UXEP	UXEP	UXEP	UXEP	UXEP	UXCEA	UXCEA	UXCEA	UXCEA	UXCEA
Item 1										
8	775	1,397	719	538	1,060	706	784	509	751	984
16	772	1,372	768	637	1,114	699	685	578	827	1,070
32	838	1,416	749	735	1,230	804	856	537	896	1,078
64	769	1,301	618	746	1,213	617	730	503	948	1,062
128	850	1,452	684	755	1,244	722	788	575	1,332	1,092
256	1,150	1,395	691	811	1,377	864	823	577	1,545	1,193
512	–	1,385	752	–	1,469	827	850	621	1,315	1,124
1,024	–	–	873	–	1,632	886	840	769	1,562	1,323
2,048	–	–	935	–	1,881	924	918	895	1,601	1,408
4,096	–	–	953	–	2,167	923	1,003	675	1,746	1,522
8,192	–	–	839	–	2,085	934	864	740	1,492	1,484
10,000	–	–	839	–	1,908	871	799	711	1,338	1,260

O = offset; C = center; T = top; B = bottom

Uniaxial strain gauge response											
Location	O	O	C	O	O	O	O	C	C	O	O
Side	T	B	B	T	B	T	B	T	B	T	B
ID	7A	7B	8B	9A	9B	10A	10B	11A	11B	12A	12B
Gauge type	UXEP	UXEP	UXEP	UXEP	UXEP	UXCEA	UXCEA	UXCEA	UXCEA	UXCEA	UXCEA
Item 2											
8	773	718	622	683	562	892	915	528	381	551	626
16	778	643	782	677	569	788	857	625	410	527	627
32	836	710	904	770	612	852	873	743	493	547	673
64	793	660	844	796	666	890	869	726	455	586	742
128	955	744	878	830	681	940	825	792	494	641	758
256	1,068	818	1,033	1,001	762	1,161	1054	950	608	750	878
512	1,280	837	1,156	1,087	788	1,161	988	1,016	810	804	912
1,024	1,497	925	1,180	1,147	850	1,306	1,221	1,107	934	953	933
2,048	–	1,066	1,267	1,200	–	1,451	1,387	1,071	1,139	969	959
4,096	–	1,254	1,190	1,224	–	1,331	1,620	1,001	1,315	1,311	1,709
8,192	–	1,268	1,042	1,216	–	1,263	1,672	891	1,318	824	894
10,000	–	1,231	1,080	1,211	–	1,121	1,583	960	1,292	722	804

O = offset; C = center; T = top; B = bottom

Acronyms

Term	Definition
AASHTO	American Association of State Highway and Transportation Officials
ASTM	American Society for Testing and Materials
BC	Base Coefficient
BE	Bender Element
CBR	California Bearing Ratio
Cc	Coefficient of Curvature
CH	High-plasticity Clay
Cu	Coefficient of Uniformity
DCP	Dynamic Cone Penetrometer
EPC	Earth Pressure Cell
ERDC	Engineer Research and Development Center
ESAL	Equivalent Single Axle Load
FWD	Falling Weight Deflectometer
IR	In-Rut
ISM	Impulse Stiffness Modulus
LL	Liquid Limit
LMS	Limestone
MD	Mid-Depth
MDD	Maximum Dry Density
OMC	Optimum Moisture Content
OR	Out-Rut
PI	Plasticity Index
PL	Plastic Limit
SDD	Single Depth Deflectometer
SN	Structural Number
USACE	United States Army Corps of Engineers
USCS	Unified Soil Classification System
USG	Uniaxial Strain Gauge
UXCEA	Uniaxial Strain Gauge Model CEA-06-125-350
UXEP	Uniaxial Strain Gauge Model EP-08-125-350

Unit Conversion Factors

Multiply	By	To Obtain
cubic feet	0.02831685	cubic meters
feet	0.3048	meters
inches	0.0254	meters
microinches	0.0254	micrometers
microns	1.0 E-06	meters
miles per hour	0.44704	meters per second
mils	0.0254	millimeters
pounds (force)	4.448222	newtons
pounds (force) per foot	14.59390	newtons per meter
pounds (force) per inch	175.1268	newtons per meter
pounds (force) per square foot	47.88026	pascals
pounds (force) per square inch	6.894757	kilopascals
pounds (mass)	0.45359237	kilograms
pounds (mass) per cubic foot	16.01846	kilograms per cubic meter
pounds (mass) per cubic inch	2.757990 E+04	kilograms per cubic meter
pounds (mass) per square foot	4.882428	kilograms per square meter
pounds (mass) per square yard	0.542492	kilograms per square meter
square feet	0.09290304	square meters
square inches	6.4516 E-04	square meters
tons (force)	8,896.443	newtons
yards	0.9144	meters

REPORT DOCUMENTATION PAGE

Form Approved
OMB No. 0704-0188

Public reporting burden for this collection of information is estimated to average 1 hour per response, including the time for reviewing instructions, searching existing data sources, gathering and maintaining the data needed, and completing and reviewing this collection of information. Send comments regarding this burden estimate or any other aspect of this collection of information, including suggestions for reducing this burden to Department of Defense, Washington Headquarters Services, Directorate for Information Operations and Reports (0704-0188), 1215 Jefferson Davis Highway, Suite 1204, Arlington, VA 22202-4302. Respondents should be aware that notwithstanding any other provision of law, no person shall be subject to any penalty for failing to comply with a collection of information if it does not display a currently valid OMB control number. **PLEASE DO NOT RETURN YOUR FORM TO THE ABOVE ADDRESS.**

1. REPORT DATE *(DD-MM-YYYY)*	2. REPORT TYPE	3. DATES COVERED *(From - To)*
March 2022	Final	

4. TITLE AND SUBTITLE

Full-Scale Evaluation of Multi-axial Geogrids in Road Applications

5a. CONTRACT NUMBER

5b. GRANT NUMBER

5c. PROGRAM ELEMENT NUMBER

6. AUTHOR(S)

W. Jeremy Robinson

5d. PROJECT NUMBER

5e. TASK NUMBER

5f. WORK UNIT NUMBER
151098

7. PERFORMING ORGANIZATION NAME(S) AND ADDRESS(ES)

Geotechnical and Structures Laboratory
U.S. Army Engineer Research and Development Center
3909 Halls Ferry Road
Vicksburg, MS 39180-6199

8. PERFORMING ORGANIZATION REPORT NUMBER

ERDC/GSL TR-22-4

9. SPONSORING / MONITORING AGENCY NAME(S) AND ADDRESS(ES)

Tensar International Corporation
Alpharetta, GA 30009-2249

10. SPONSOR/MONITOR'S ACRONYM(S)

11. SPONSOR/MONITOR'S REPORT NUMBER(S)

12. DISTRIBUTION / AVAILABILITY STATEMENT

Approved for public release; distribution is unlimited.

13. SUPPLEMENTARY NOTES

Funding Account Code 887K5B

14. ABSTRACT

The U.S. Army Engineer Research and Development Center (ERDC) constructed a full-scale unsurfaced test section to evaluate the performance of two prototype geogrids, referred to as NX950 and NX750, in road applications. The test section consisted of a 10-in.-thick crushed aggregate surface layer placed over a very weak 2 California Bearing Ratio (CBR) clay subgrade. Simulated truck traffic was applied using one of ERDC's specially designed load carts outfitted with a single-axle dual wheel truck gear. Rutting performance and instrumentation response data were monitored at multiple traffic intervals. It was found that the prototype geogrids improved rutting performance when compared to the unstabilized test item, and that the test item containing NX950 had the best rutting performance. Further, instrumentation response data indicated that the geogrids reduced measured pressure and deflection near the surface of the subgrade layer. Pressure response data in the aggregate layer suggested that the geogrids redistributed applied pressure higher in the aggregate layer, effectively changing the measured stress profile with an increase in pavement depth.

15. SUBJECT TERMS

Geogrids
Accelerated pavement testing
Trucks--Weight--Measurement
Unsurfaced road performance
Traffic benefit ratio
Base Course Stabilization
Clay soils
Unpaved road
InterAx
Pavements--Performance
Pavements--Testing

16. SECURITY CLASSIFICATION OF:			17. LIMITATION OF ABSTRACT	18. NUMBER OF PAGES	19a. NAME OF RESPONSIBLE PERSON
a. REPORT	b. ABSTRACT	c. THIS PAGE			19b. TELEPHONE NUMBER *(include area code)*
Unclassified	Unclassified	Unclassified	SAR	81	